Changes in Atlantic Water circulation in the central Arctic Ocean between 2011 and 2021 inferred from tracer observations

Anne-Marie Wefing[1,2], Annabel Payne[1], Marcel Scheiwiller[1], Christof Vockenhuber[1,3], Marcus Christl[3], Toste Tanhua[4], and Núria Casacuberta[1,3]

[1]Department of Environmental Systems Science, ETHZ, Zurich, Switzerland
[2]Norwegian Polar Institute, Tromsø, Norway
[3]Laboratory of Ion Beam Physics, ETHZ, Zurich, Switzerland
[4]GEOMAR Helmholtz Centre for Ocean Research Kiel, Kiel, Germany

Correspondence: Anne-Marie Wefing (annemarie.wefing@npolar.no)

Abstract. Atlantic Water circulation and associated changes play a crucial role in the future of the Arctic Ocean, especially in light of ongoing "Atlantification" trends. Still, the pathways, mixing properties, and circulation times of Atlantic Water in the Arctic Ocean remain to be better understood in view of recent variability and trends. Here, we use the long-lived anthropogenic radionuclides I129 and U236 to investigate mixing between Atlantic and Pacific Waters in the surface layer and to determine Atlantic Water circulation times and mixing in the mid-depth Atlantic layer of the Arctic Ocean using the Transit Time Distribution (TTD) model. The study is mainly based on radionuclide data that has been collected in the central Arctic Ocean during the "SAS-Oden 2021" expedition aboard the Swedish research icebreaker *Oden*, which was part of the Synoptic Arctic Survey (SAS) programme. Furthermore, to assess temporal changes in the circulation pattern and circulation times of Atlantic Water between 2011 and 2021, we use available historic data on I129 and U236 between 2011 and 2021. For 2021, we find a sharp decrease in surface I129 and U236 concentrations between the Amundsen and Makarov Basins, pointing to significant fractions of Pacific Water reaching the Lomonosov Ridge from the Amerasian side. In the halocline layer below, similar and comparably high I129 and U236 concentrations suggest a similar formation region of halocline waters with a clear Atlantic Water signal. North of Greenland, we find a mixture of waters that originate from the Canada and Amundsen basins, both in the surface and the mid-depth layer. The TTD model shows higher circulation times pointing to a longer transport route on the Makarov Basin side of the Lomonosov Ridge. Regarding temporal changes, we find a shift in the location of the Atlantic-Pacific Water front from 2011/12, when it was located further into the Makarov Basin, to 2015 and 2021. In the mid-depth Atlantic layer, mean and mode ages show an increase from 2015 to 2021, which is in line with recent studies based on gas tracers and suggests a slowdown or changes in the pathways of the Arctic Ocean Boundary Current.

1 Introduction

1.1 Changing Arctic Ocean circulation

The Arctic region is undergoing rapid changes as a result of anthropogenic climate change, including an unprecedented warming trend with temperature increases that are four times higher than the global average (Rantanen et al., 2022). Especially relevant for the Eurasian Basin of the Arctic Ocean is the so-called "Atlantification", the expansion of warm Atlantic inflows into the Arctic, contributing to the observed sea-ice decrease and weakening stratification (Polyakov et al., 2005, 2017). Recently, an increased oceanic heat flux from warm Atlantic Water at intermediate depths to the surface layer and sea ice has been observed, associated with a thinned halocline layer (Polyakov et al., 2020). Wang et al. (2024) found the ongoing sea ice decline (e.g., Kwok, 2018) to act as a primary driver of the atlantification of the Eurasian Basin in the 2010s. Furthermore, the recent study by Polyakov et al. (2025) showed that atlantification is not limited to the Eurasian Arctic anymore, but also observed beyond the Lomonosov Ridge in the Makarov Basin.

Atlantic Water enters the Arctic Ocean via two gateways, Fram Strait and the Barents Sea. Both branches are cooled along their northward passage and converge in the St Anna Trough region. From here, the Fram Strait Branch Water (FSBW) and the Barents Sea Branch Water (BSBW) circulate through the Arctic Ocean along different loops, forming the Arctic Ocean Boundary Current (AOBC). Part of the Atlantic Water recirculates to Fram Strait within the Eurasian Basin and part of it enters the Amerasian Basin following a longer loop before also exiting through Fram Strait. Pacific Water enters the Arctic Ocean through Bering Strait and is restricted to the upper layer due to its lower density compared to Atlantic Water and mainly resides in the Canada and Makarov basins (e.g., Rudels, 2015) (Fig. 1).

The water column in the Arctic Ocean can be divided into different layers containing waters of different origin. The upper layer, here referred to as Polar Surface Water (PSW), is colder and fresher than the underlying warmer and more saline Atlantic Water. The PSW layer is highly stratified and generally entails Pacific Water, river runoff, sea-ice meltwater, as well as transformed Atlantic Water. It can be further divided into the Polar Mixed Layer (PML) at the surface, defined by the temperature minimum that is a remnant of the previous winter convection forming a deeper mixed layer (Korhonen et al., 2013), and the halocline layer below. In the Eurasian Basin, the transition between the PML and the deeper Atlantic Water with temperatures above $0°C$ is formed by the lower halocline (LHC). The LHC originates from the cooling and freshening of Atlantic Water north of Fram Strait and the Barents Sea (Rudels et al., 1996; Korhonen et al., 2013). In the Amerasian Basin, the halocline consists of an additional layer between the PML and the LHC, the upper halocline (UHC). The UHC mainly consists of low salinity Pacific Water inflow through Bering Strait and Siberian river runoff (Korhonen et al., 2013).

The Arctic Ocean plays a crucial role in the global oceanic circulation through the Atlantic Meridional Overturning Circulation (AMOC), and changes in Arctic circulation will therefore be conveyed beyond the Arctic region (e.g., Le Bras et al., 2021). The role of Atlantic Water circulation in the Arctic Ocean and associated changes have been investigated through var-
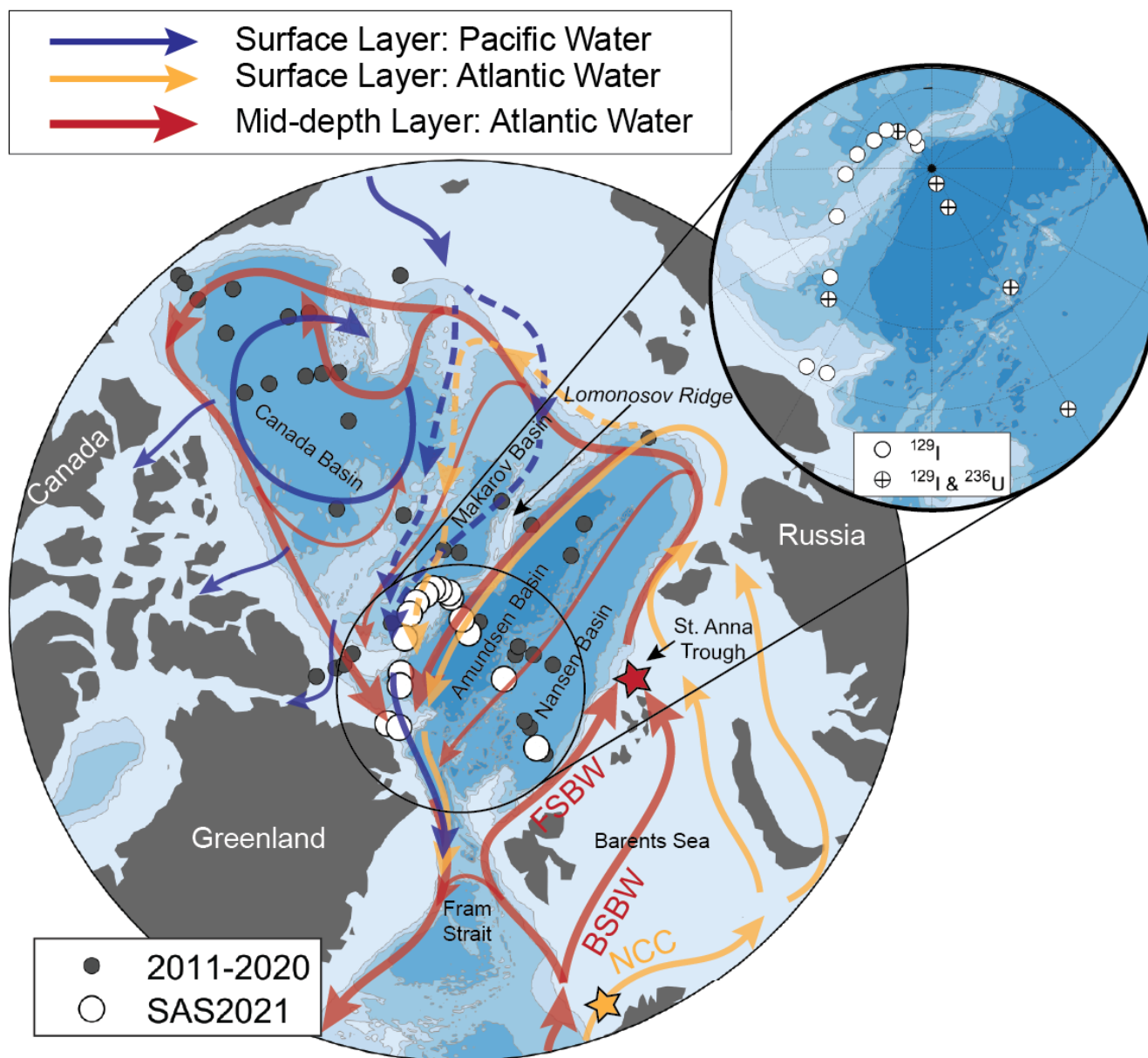
Figure 1. Map of the Arctic Ocean with main topographic and circulation features, as well as stations of radionuclide samples considered in this study. Blue and orange arrows show circulation patterns of Pacific and Atlantic Water in the surface, respectively, red arrows show circulation of Atlantic Water at mid-depth. FSBW: Fram Strait Branch Water, BSBW: Barents Sea Branch Water, NCC: Norwegian Coastal Current. The yellow and red star denote the locations where the surface layer input function (yellow, southern Barents Sea Opening) and mid-depth Atlantic layer input function (red, St. Anna Trough) were defined (see Fig. 2). Stations with published I129 and U236 data from earlier years (2011-2020) are shown in dark grey, see Section 2.1 for details. Radionuclide stations from SAS2021 are shown in white, with the inset further distinguishing stations where only I129 data is available (white circles) and stations where I129 and U236 data is available (white circles with black cross).

ious methods, including modeling studies (e.g., Wang et al., 2024), extensive hydrographic measurements (e.g., Schulz et al., 2024), as well as tracer studies (e.g., Tanhua et al., 2009; Gerke et al., 2024; Körtke et al., 2024). As part of the latter, anthropogenic radionuclides labeling Atlantic Water have proven to be valuable tools (e.g., Smith et al., 2021; Casacuberta and Smith, 2022). In recent years, the two radionuclides I129 and U236 have been utilized as Atlantic Water tracers in several studies. The combination of I129 and U236 provided a better understanding of Atlantic Water pathways (Casacuberta et al., 2018), Atlantic Water circulation times and changes therein (Wefing et al., 2021), mixing within the flow field (Payne et al., 2024), the uptake of anthropogenic carbon by Atlantic Waters (Raimondi et al., 2024), as well as mixing of different water masses and freshwater components in waters outflowing the Arctic through Fram Strait (Wefing et al., 2022). Here, we build on these works using the available historic I129 and U236 data from the Arctic Ocean together with new data collected in 2021, to investigate the distribution of different water masses in 2021 and assess decadal changes in Atlantic Water circulation since 2011.

1.2 Anthropogenic radionuclides I129 and U236 as tracers of circulation changes

I129 and U236 are long-lived radionuclides with half-lives of about 16 Myr and 23 Myr, respectively. They have been introduced into the marine environment by two sources, both of anthropogenic origin. Firstly, liquid releases from nuclear reprocessing plants, which introduced mainly I129, and secondly, via global fallout from atmospheric nuclear weapon tests, which introduced mainly U236 (Casacuberta et al., 2016). In the Arctic Ocean, releases from the two European reprocessing plants, Sellafield in the UK, and La Hague in France, are the dominant source of 129I and 236U, followed by the global fallout signal (only relevant for U236). The natural background of these two radionuclides is many orders of magnitude lower than the inputs from anthropogenic activities (Casacuberta et al., 2016).

The liquid releases of I129 and U236 from the two European reprocessing plants are transported northwards from the North Sea to the Arctic Ocean mainly by the Norwegian Coastal Current (NCC) (Edmonds, 2001; Gascard et al., 2004; Smith et al., 2011; Christl et al., 2015b, Fig 1). The global fallout signal is found in all water masses and introduced into the Arctic Ocean by both Atlantic and Pacific Water. The tracer signal carried by the NCC is also mixed into surrounding Atlantic Water during its northward passage, and hence all Atlantic Water entering the Arctic Ocean is tagged with a distinct tracer signature of I129 and U236 (Casacuberta et al., 2018, see also Section 2.2 for details). The concentration of I129 and U236 introduced by Pacific Water (global fallout signal) and its distribution in the Canada Basin has been assessed in the recent study by Payne et al. (2024).

Classically, gas tracers such as CFCs and SF_6 have been used to study changes in Atlantic Water circulation, with a focus on ventilation timescales since these tracers are introduced by air-sea gas exchange (e.g., Tanhua et al., 2009; Körtke et al., 2024). The recent study by Gerke et al. (2024) based on CFC-12 and SF_6 data from the Eurasian Basin collected between 1991 and 2021 found higher mean ages in 2021 compared to earlier years in the Amundsen Basin. This implies a decrease in ventilation, which was found to have happened primarily over the past 16 years and the authors speculate about a possible decrease in the

strength of the AOBC, increasing transport times of Atlantic Water.

In contrast to I129 and U236, CFCs and SF_6 have a global atmospheric source and can, therefore, be applied to investigate
90   ventilation dynamics throughout the world's oceans. I129 and U236 are most powerful in the Arctic Ocean and the subpolar
North Atlantic, but have the advantage that they can also be used to asses circulation times in the surface layer, which is in
contact with the atmosphere. For the comparison of gas tracers and radionuclides, the Arctic Ocean provides a unique con-
figuration, since Atlantic Waters are isolated from atmospheric exchange once they subduct to depths and are capped by the
halocline layer (see also Raimondi et al. (2024) for further discussion). With the rapid changes occurring in the Arctic Ocean,
95   on the order of decades or below, available historical I129 and U236 data can now be used to assess temporal changes in
Atlantic Water circulation (Smith et al., 2021), to complement other tracer, hydrographic, and model studies.

In this study, we use I129 and U236 data collected in the central Arctic Ocean in 2021 to investigate Atlantic Water pathways,
mixing between Atlantic and Pacific Waters and other end-members in the surface layer, as well as Atlantic Water circulation
100   times. We place a special focus on the Lincoln Sea north of Greenland, where waters from the Amerasian and Eurasian basins
converge before exiting the Arctic through the Nares or Fram Strait. Furthermore, we assess temporal changes in the circulation
pattern and circulation times of Atlantic Water between 2011 and 2021. This contributes to the understanding of how changes
in the Atlantic Waters entering the Arctic Ocean affect the Arctic system.

2   Material and Methods

105   ### 2.1   Radionuclide Tracer Data

Seawater samples for the analysis of I129 and U236 were collected in 2021 during the "SAS-Oden 2021" expedition (SAS2021)
aboard the Swedish research icebreaker *Oden* (Snoeijs-Leijonmalm et al., 2022), which was part of the Synoptic Arctic Survey
(SAS). Hydrographic data from CTD profiles for this expedition is available on PANGAEA (Heuzé et al., 2022a). Biogeo-
chemical bottle data is available both on PANGAEA (Heuzé et al., 2022b) and published in GLODAPv2.2023 (Lauvset et al.,
110   2024). In total, 167 samples (16 full-depth stations) were taken for I129 analysis and 48 samples (6 full-depth stations) were
taken for U236 analysis at several stations along the cruise track from north of Svalbard towards the North Pole and further
towards northern Greenland (Fig. 1). Samples were filled directly from the Niskin bottles mounted on the CTD-rosette into
rinsed plastic 250 mL bottles (for I129 analysis) and 3 L plastic cubitainers (for U236 analysis) and shipped to ETH Zurich,
Switzerland, for radionuclide analysis.

115

I129 analysis followed the method of Casacuberta et al. (2016), also described in Payne et al. (2024). Samples were measured
by Accelerator Mass Spectrometry (AMS) using the 0.5 MV AMS system *TANDY* at the Laboratory of Ion Beam Physics at
ETH Zurich, Switzerland (Vockenhuber et al., 2015). Concentrated and diluted forms of an in-house standard, C2, were in-
cluded with each measurement run (nominal value diluted: 129I/127I = 5.055×10^{-12} at at^{-1}, nominal value concentrated:

Table 1. Information on published radionuclide data from earlier expeditions used in this study.

Year	Cruise	Ship	Tracers	References
2011	PS78	RV Polarstern	I129, U236	Casacuberta et al. (2016); Wefing et al. (2021)
2012	PS80	RV Polarstern	I129, U236	Casacuberta et al. (2016); Wefing et al. (2021)
2012	Switchyard/LDEO	*aircraft*	I129	Smith et al. (2021); Casacuberta and Smith (2022)
2015	PS94	RV Polarstern	I129, U236	Casacuberta et al. (2018); Wefing et al. (2021); Raimondi et al. (2024)
2015	HLY1502	USCGC Healy	I129, U236	Smith et al. (2021); Chamizo et al. (2022); Raimondi et al. (2024)
2020	JOIS2020	CCGS Louis St Laurent	I129, U236	Payne et al. (2024)

120 129I/127I = 38.995×10^{-12} at at^{-1}). All samples were corrected with chemistry blanks ($n = 12$) prepared in the lab at ETH Zurich (MilliQ water, $18.2\ \mathrm{M\Omega}$). Relative uncertainties are largely around 3 %, based on the analytical uncertainty of the AMS measurement and repeated measurements of an ETH internal standard (standard deviation of 2 %, $n = 6$).

U236 analysis followed the method of Christl et al. (2015a) and has also been described in Payne et al. (2024). Samples

125 were measured using the 0.3 MV AMS system *MILEA* at the Laboratory of Ion Beam Physics at ETH Zurich, Switzerland (Christl et al., 2023). Measured isotope ratios were normalized to the in-house standard ZUTRI (nominal values: 233U/238U = $(33,170 \pm 830) \times 10^{-12}$ at at^{-1}, 236U/238U = $(4,055 \pm 200) \times 10^{-12}$ at at^{-1}) (Christl et al., 2013). U236 and U238 concentration were calculated from the measured concentration of the U233 spike. All samples were corrected with chemistry blanks ($n = 5$) prepared in the lab at ETH Zurich (MilliQ water, $18.2\ \mathrm{M\Omega}$). Relative uncertainties are largely around 3 %, based on

130 the analytical uncertainty of the AMS measurement and assuming the same standard deviation of repeated measurements as for I129.

I129 and U236 data from SAS2021 are available on Zenodo (Wefing, 2025). To assess temporal changes over the past decade, we used published radionuclide data from several past expeditions to the Arctic Ocean, which are listed in Table 1 with

135 references for corresponding radionuclide data.

2.2 Tracer Input Functions

Input functions of I129 and U236 describe the concentrations of both tracers entering the Arctic Ocean at a defined initialization point over time (Fig. 2). Here, we used the input functions defined and described in Wefing et al. (2021), which were also used

140 in Raimondi et al. (2024) and Payne et al. (2024). Briefly, one input function for each radionuclide was defined for the surface layer, describing the concentrations of both tracers in Atlantic-origin Water that is transported with the Norwegian Coastal Current over the shelf seas (Barents, Kara, and Laptev Sea) and enters into the Polar Surface Water. The initialization point for
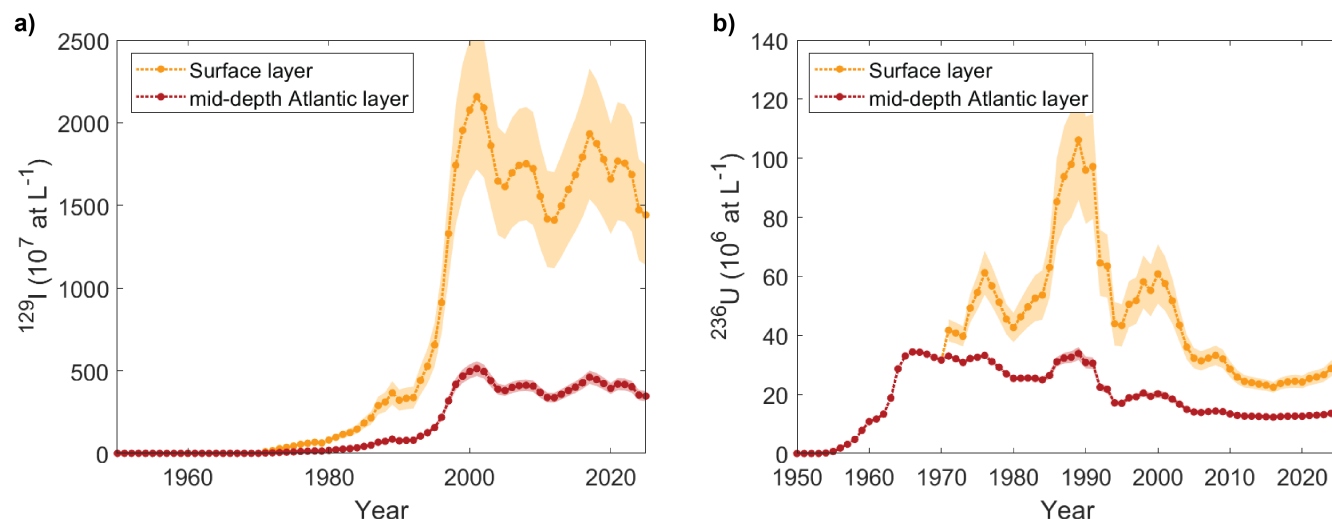
Figure 2. Input functions of I129 (a) and U236 (b) for the surface and mid-depth Atlantic layer, defined for the northern Norwegian Coast and the St. Anna Trough, respectively. Locations are marked with stars in Fig. 1. Shaded areas are the uncertainties of each input function.

the surface layer input functions lies at around 72°N at the Barents Sea Opening, north of the Norwegian Coast (orange star in Fig. 1). A different input function for I129 and U236 was defined for the Atlantic layer, describing the concentrations of both tracers in Atlantic Water (FSBW and BSBW) forming the mid-depth Atlantic-origin layer of the Arctic Ocean. For the Atlantic layer input function, we consider the St. Anna Trough as the initialization point, since this is the location where FSBW and BSBW subduct and jointly form the Atlantic layer further downstream in the Arctic Ocean (red star in Fig. 1).

2.3 Tracer ages and Transit Time Distributions

A Binary Mixing Model with I129 and U236 was applied to investigate mixing between different end-members and to determine radionuclide-based tracer ages in PSW. Details are given in Wefing et al. (2021). Note that this is a simple model assuming purely advective flow.

The Transit Time Distribution (TTD) method was applied to describe the characteristics of Atlantic Water circulation in the mid-depth layer of the Arctic Ocean. This model has mainly been applied to ocean interior ventilation studies (e.g., Haine and Hall, 2002; Waugh et al., 2003; Tanhua et al., 2009; Stöven et al., 2015) and to determine anthropogenic CO_2 uptake by the ocean (e.g., Waugh et al., 2006; Khatiwala et al., 2013; Stöven and Tanhua, 2014; Stöven et al., 2016; Raimondi et al., 2024; Gerke et al., 2024). Its use with anthropogenic radionuclides has been investigated in several recent studies (Smith et al., 2011; Wefing et al., 2021; Smith et al., 2021) and the application to the I129-U236 tracer pair have been extensively described in Raimondi et al. (2024, therein referred to as "Smith's TTD approach"). Therefore, we will only provide a brief summary here.

In the TTD model, the concentration of a stable tracer at sampling location x and time t is described by

$$c(x,t) = \int_0^\infty c_0\left(t - t'\right) G\left(x, t'\right) dt' \tag{1}$$

where c_0 represents the tracer input function and $G(x,t)$ is the Green's function which describes the propagation of the tracer signal and, therefore, the characteristics of the flow from the initialization of the input function to the sampling location. G is essentially a probability density function (PDF) reflecting the weight of tracer signals from different years of the input function at the specified sampling location and time. The flow is limited to 1D for simplicity, and in this case, the PDF is given by an inverse Gaussian function:

$$G(x,t) = \sqrt{\frac{\Gamma^3}{4\pi \Delta^2 t^3}} \, exp\left(-\frac{\Gamma(t-\Gamma)^2}{4\Delta^2 t}\right) \tag{2}$$

defined by two parameters, Γ and Δ. Γ represents the mean age of the distribution while Δ is a measure of the width of the PDF, and hence describes how much a tracer signal disperses during the flow as a result of lateral mixing. $\Delta = 0$ corresponds to purely advective flow. Another age measure of the distribution is the mode age t_{mode} (also termed most probable age, Smith et al., 2011; Wefing et al., 2021), the circulation time with the highest probability within the PDF. It is given by

$$t_{mode} = \frac{1}{\Gamma}\left(\sqrt{9\Delta^4 + \Gamma^4} - 3\Delta^2\right) \text{ with } t_{mode} \geq 1. \tag{3}$$

In the case of a mixture of two water masses that can each be described by a TTD, we consider a linear combination of two inverse Gaussian TTDs $G_1\left(\Gamma_1, \Delta_1\right)$ and $G_2\left(\Gamma_2, \Delta_2\right)$ (Waugh et al., 2003; Smith et al., 2022):

$$G_{mix} = \alpha G_1\left(\Gamma_1, \Delta_1\right) + (1 - \alpha) G_2\left(\Gamma_2, \Delta_2\right) \tag{4}$$

where α describes the fraction of the water mass described by $G_1\left(\Gamma_1, \Delta_1\right)$ in the mixture.

2.4 Water mass classification

Water mass classifications used in this study followed the definition by Marnela et al. (2008) for the general water masses and (Korhonen et al., 2013) for the PSW (PML, UHC, LHC). Samples were generally divided into Polar Surface Water (PSW, $\sigma_\Theta < 27.70$) and Arctic Atlantic Water (AAW, $27.70 \leq \sigma_\Theta < 27.97$), as well as the intermediate ($27.97 \leq \sigma_\Theta$, $\sigma_{0.5} < 30.444$), and deep ($30.444 \leq \sigma_{0.5}$) layer. The PSW samples were further divided into the Polar Mixed Layer (PML, lower boundary defined by the temperature minimum that is a remnant of the previous winter convection forming a deeper mixed layer), and the halocline layer. For samples from the Eurasian Basin, we only considered the lower halocline layer (LHC, from lower boundary of the PML down to $\Theta = 0°$ C). For samples from the Amerasian Basin, we considered an additional upper halocline layer between PML and LHC as described in Section 1.1 (UHC, from lower boundary of the PML down to $S_p = 34$).

3 Results

In the results section, we will first show the distribution of I129 and U236 in depth profiles and along the SAS2021 transect and then put the I129 results in relation to hydrographic parameters. Note that we restrict the second part to I129 data, due to the larger dataset compared to U236.
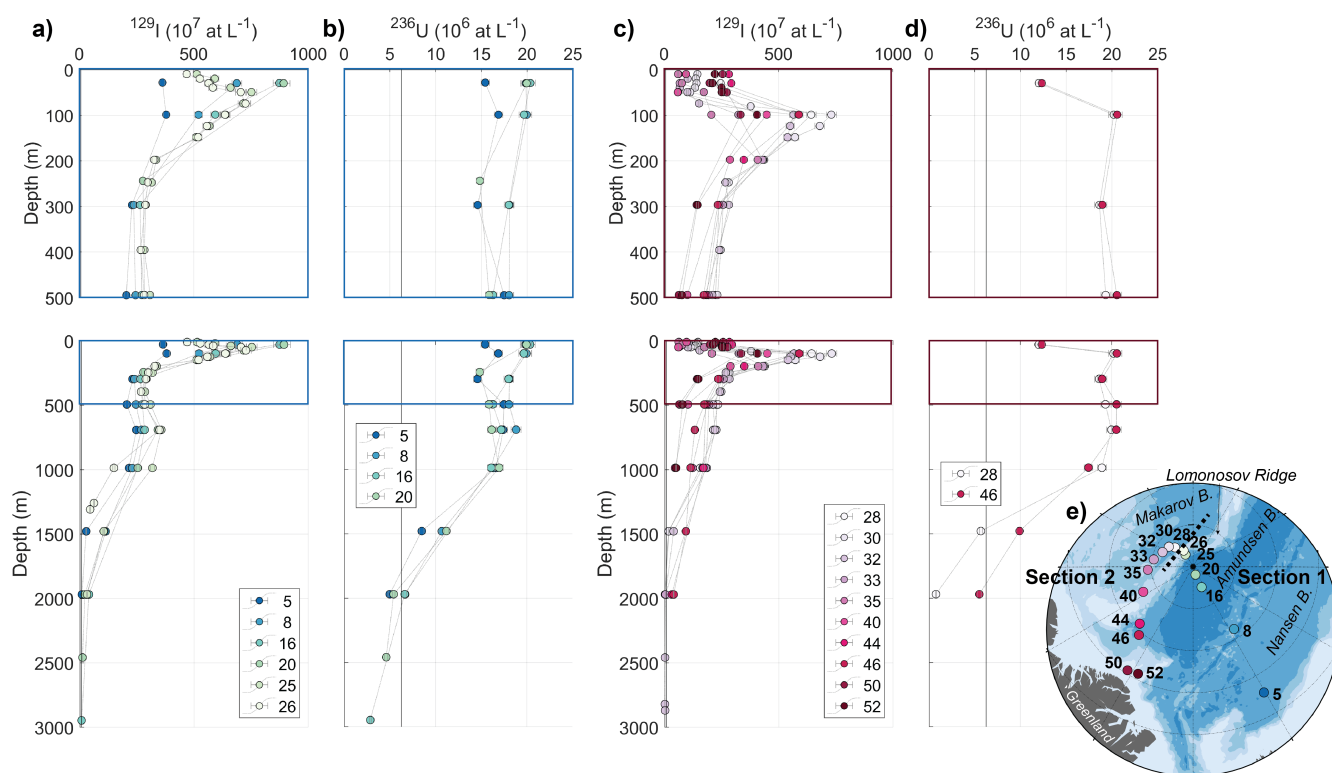
3.1 Distribution of I129 and U236

Figure 3. Depth profiles of 236U and 129I concentrations for all SAS2021 stations from Section 1 (a: I129, b: U236) and Section 2 (c: I129, d: U236). Top row is a close up of 0-500 m, marked by the box in the full-depth profiles in the bottom row. Black vertical lines indicate global fallout background signal for both radionuclides from Payne et al. (2024). Note that it is not distinguishable from zero in the I129 profiles (panels a and c). (e) Map showing stations classified as Section 1 (blue-green colors) and 2 (red-purple colors). The dashed line indicates the division between both sections.

I129 and U236 concentrations are presented in profiles, divided into two sections of the expedition (Fig. 3), and as section plots (Fig. 4, only upper 200 m). Section 1 comprises stations from the Nansen and Amundsen Basins up to the Lomonosov Ridge, whereas Section 2 comprises stations from the Makarov Basin and the region north of Greenland (Fig. 3e).
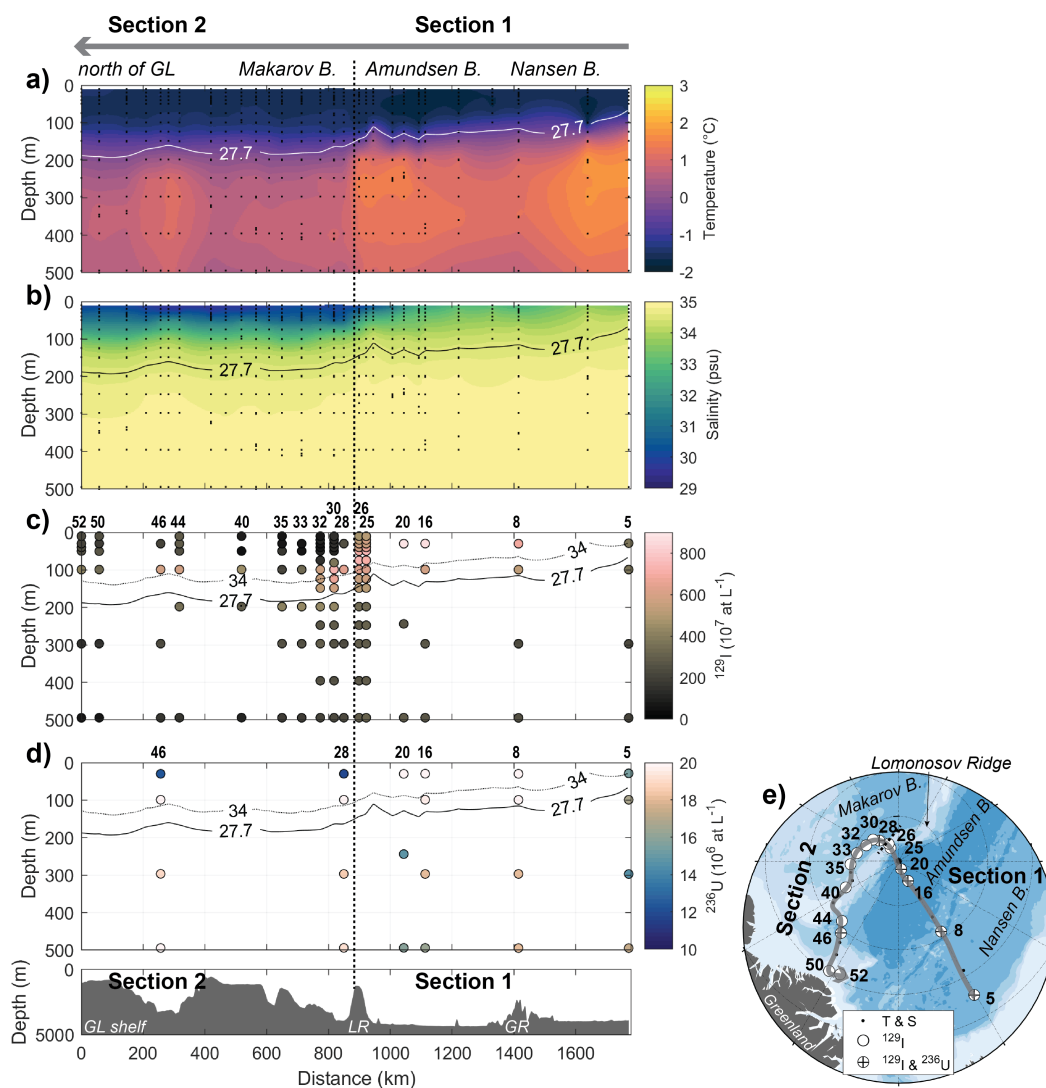
Figure 4. Section plots (upper 500 m) of CTD temperature (a), practical salinity (b), I129 (c), and U236 concentration (d), following the cruise track from the Nansen Basin (right-hand side of plots) to the Lomonosov Ridge (middle) and the Greenland shelf (left-hand side of plots). Continuous line is $\sigma_\Theta = 27.7$, dashed line in c and d is the isoline of practical salinity 34. Seafloor topography from GEBCO (GEBCO Compilation Group, 2024) is shown below the section plots, indicating the Greenland shelf (GL shelf), the Lomonosov Ridge (LR), and the Gakkel Ridge (GR). The transect is indicated as a grey line in the station map (e).

For all profiles from Section 1, the highest I129 concentrations were observed in the upper 100 m, with a peak in I129 at 50-100 m for stations 25 and 26 (around 700×10^7 at L^{-1}, note the higher depth resolution for both stations) and a peak at

200 around 50 m for stations 16 and 20 (around 900×10^7 at L^{-1}) (Fig. 3a). At all stations, I129 concentrations decreased with depth down to 500 m and increased again to a local maximum around 700 m (between 200×10^7 at L^{-1} and 400×10^7 at L^{-1}). Below 700 m, concentrations decreased further to almost 0 in the deepest samples at 3000 m depth. Generally, within the upper 1000 m, higher concentrations were observed at stations further north. Station 5 (located in the Nansen Basin) showed the lowest I129 concentrations throughout the entire depth range (except for station 26 at 1000 m and below), especially in the upper

205 100 m. I129 concentrations at Station 8 (at the Gakkel Ridge) were in between those from station 5 and station 16. Station 26 (on top of the Lomonosov Ridge) showed the highest I129 concentrations among all Section 1 stations between depths of 100 to 700 m, but concentrations decreased sharply between 700 and 1000 m. In contrast to I129, U236 concentrations across Section 1 (note lower spatial and depth resolution) did not exhibit much variability in the upper 1000 m ($15 - 20 \times 10^6$ at L^{-1}) and no clear trend was observed among different stations (Fig. 3b). No apparent peak in U236 concentrations was observed

210 at 50-100 m, however, the sampling resolution was lower compared to I129. Similar to I129, a slight local maximum was observed at 700 m depth. U236 concentrations reached global fallout levels at around 2000 m depth and decreased further to around 3×10^6 at L^{-1} at 3000 m depth.

For Section 2, the shape of I129 profiles was different from Section 1 in the upper 500 m. The maximum of I129 concentra-

215 tions ($200 - 700 \times 10^7$ at L^{-1}) was found around 100 m depth for all Section 2 stations, therefore, at greater depths than for Section 1 (Fig. 3c). Towards the surface, concentrations decreased to around $100 - 300 \times 10^7$ at L^{-1}. Surface I129 concentrations of all Section 2 stations were lower than those from Section 1, and the overall lowest I129 concentrations were observed for stations in the Makarov basin. Generally, as for Section 1, profiles further to the north exhibited higher concentrations (above 1000 m). U236 data was only analyzed for two stations from Section 2. Both profiles were very similar in the upper

220 1000 m (Fig. 3d). Above 100 m depth, U236 concentrations decreased towards the surface, similar to I129, but in contrast, were almost constant over the depth range of 100-1000 m. station 28 (in the Makarov Basin) showed a significantly lower U236 concentration (almost 0) at 2000 m than all other stations (including those from Section 1).

Considering the transition from Section 1 to Section 2 in particular (station 26 to 28, only I129 data is available for both,

225 brightest colors in Fig. 3), we observed a clear drop in I129 from station 26 to 28, i.e., from the Amundsen to the Makarov Basin, at depths of around 50 m and between 500 and 1000 m (especially at 700 m). In contrast, between 50 and 500 m depth, concentrations were similar at both stations. Differences in upper layer I129 and U236 between Section 1 and Section 2 are also visible in the section plots covering both sections (Fig. 4). Especially the decline in I129 and U236 above 100 m in Section 2 (left half of the sections) is well noticeable, coinciding with a decrease in salinity at the same depths. To further examine the

230 relation of radionuclide concentrations with hydrographic parameters and different water masses in the SAS2021 study area, we will focus on I129 in the following section due to the better spatial coverage for this radionuclide.

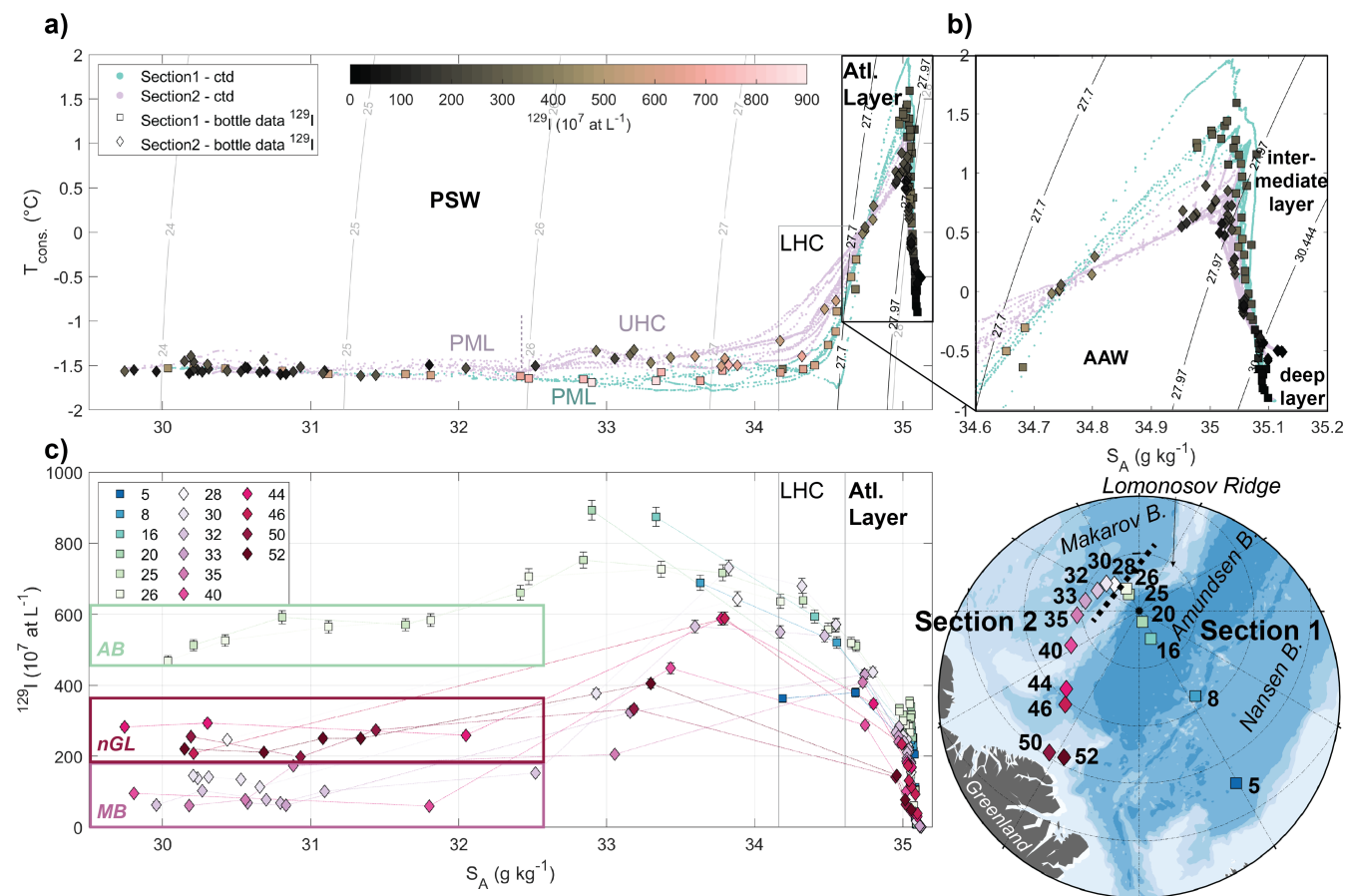## 3.2 I129 in relation to hydrographic parameters

Figure 5. (a) T-S plot (conservative temperature against absolute salinity) with I129 concentrations color-coded and different water masses indicated (PSW: Polar Surface Water, PML: Polar Mixed Layer, UHC: upper halocline, LHC: lower halocline, AAW: Arctic Atlantic Water). Teal and purple dots are 1 m-binned ctd data from Section 1 and 2, respectively. Square and diamond data points are bottle file data from Section 1 and 2, respectively. (b) close-up of the Atlantic Layer (black box in a). (c) Plot of I129 concentration against absolute salinity with stations color-coded. AB: Amundsen Basin, nGL: north of Greenland, MB: Makarov Basin.

In the T-S plot (Fig. 5a, conservative temperature against absolute salinity, different water masses are highlighted following
235   Section 2.4) the two sections of the expedition showed different features: PSW from Section 2 had slightly higher temperatures
compared to Section 1, especially for salinities above 32 (see also Section 4.1.2). In AAW and below, the opposite was ob-
served, with Section 1 stations showing higher temperatures compared to Section 2 (Fig. 5b). Highest AAW temperatures were
observed at station 5 in the Nansen Basin, closest to the Atlantic Water inflow region. I129 (color-coded) was high throughout

the entire PSW in Section 1 and highest in the LHC for Section 2.

240

The distribution of I129 in the different water masses and layers is best shown in a plot of I129 concentration against salinity (Fig. 5c). At salinities < 32 (PML), highest I129 concentrations ($400 - 600 \times 10^7$ at L^{-1}) were found in samples from the Amundsen Basin (Section 1), followed by the stations north of Greenland (Section 2, $200 - 300 \times 10^7$ at L^{-1}). Makarov Basin stations (also Section 2) exhibited the lowest I129 concentrations ($0 - 200 \times 10^7$ at L^{-1}) for salinities < 32. Note that in this salinity range, the two sections of the expedition could not be distinguished well in T-S space (apart from station 50 showing higher temperatures at salinities between 30 and 31). In contrast, the three sampling regions of the Amundsen Basin (Section 1), the Makarov Basin (Section 2), and the stations north of Greenland (Section 2) differed significantly in I129, suggesting differences in the proportions of Atlantic-origin water carrying the tracer signal (see Section 4.1.1 for further discussion). In general, concentrations were more variable throughout the PML in Section 1, also within the same station (Fig. 5c). Note that the PML in Section 1 extended to practical salinity 34 and there was no UHC layer, but we still observed a change in I129 at a salinity of around 32.5, approximately coinciding with the upper limit of the UHC layer in Section 2.

The highest I129 concentrations of the entire SAS2021 dataset were found in Amundsen Basin stations in the salinity range 32-34, corresponding to the lower PML in Section 1 (Fig. 5c). For Section 2, the same salinity range corresponds to UHC waters and here, an increase in I129 concentrations with increasing salinity was observed. The highest I129 concentrations in Section 2 corresponded to the transition between UHC and LHC, i.e., around a salinity of 34. In contrast to the lower salinity range (PML), in the UHC layer (salinities between 32.5 and 34), samples from north of Greenland showed similar I129 concentrations compared to those from the Makarov Basin. In the LHC (salinities > 34 but $\sigma_{\Theta} < 27.7$), the few available samples from the Amundsen (Section 1) and Makarov Basins (Section 2) had similar I129 concentrations (no samples from the stations north of Greenland were available for I129 in this salinity range). Note the low I129 concentration of station 5 in the Nansen Basin, likely reflecting the tracer concentration carried by inflowing FSBW (see Section 4.1.1 for further explanation).

For samples from the Atlantic and intermediate layers close to the temperature maximum (salinities around 35), differences in I129 between both sections were observed (Fig. 5c). At similar salinities, samples from Section 1 showed higher I129 concentrations, with a clear trend of decreasing I129 from the Lomonosov Ridge (stations 25 and 26) towards the Nansen Basin (station 5, also observed in 3). Also, among stations from Section 2, the highest I129 concentrations were found close to the Lomonosov Ridge (stations 28 and 30) and decreased towards the north of Greenland. However, note the decrease in I129 in AAW at the Lomonosov Ridge (between station 26 and 28, from the Amundsen to the Makarov Basin), which was also well observed in the profiles at depths between 500 and 100m (Fig. 3a and c). The lowest I129 concentrations in AAW within Section 2 were found in Stations 50 and 52, close to Greenland. For U236 (Fig. A1), a different trend between Section 1 and Section 2 was apparent. Here, in AAW and below, stations from Section 2 had higher U236 concentrations compared to stations from Section 1 and the highest U236 concentration was found in station 46. The distribution of I129 and U236 in the Atlantic

Water layer will be further discussed in Section 4.1.1).

275 ## 4 Discussion

In the discussion, we will first highlight different aspects of the circulation of Atlantic Water in 2021 and then put these findings into the perspective of temporal changes based on previous tracer data (I129 and U236) collected across the Arctic Ocean since 2011.

4.1 Atlantic Water Circulation in the Arctic Ocean in 2021

280 #### 4.1.1 Circulation timescales in the surface layer

Atlantic Water tracer ages and information on the dilution of the Atlantic Water tracer signal were obtained from a binary mixing model in U236-I129 tracer space (Fig. 6, see also Casacuberta et al. (2018); Wefing et al. (2021); Dale et al. (2024)). Here, PSW samples are shown on top of mixing lines between the surface layer tracer input function and the steady-state global fallout signal. Each mixing line reflects the dilution of the tracer signal carried into the Arctic Ocean by Atlantic Water in a spe-
285 cific year (described by the input function), with waters carrying only the global fallout signal (taken from Payne et al. (2024)). The latter can either reflect a fraction of Atlantic Water not tagged with the reprocessing plants' tracer signal (Section 1.2) or Pacific Water that entered the Arctic Ocean through Bering Strait. Tracer ages of Atlantic Water (i.e., the time it took a water parcel to travel from the initialization point of the input function to the sampling location) are determined by finding the binary mixing line closest to the sample and correspond to the difference between sampling year and input function year. Note
290 that this is a simple model assuming purely advective flow of Atlantic Water and the presence of only two end-members in U236-I129 tracer space, but earlier studies have shown that it yields reasonable results for circulation times in the surface layer of the Arctic Ocean (Smith et al., 2011; Wefing et al., 2021).

In the dual-tracer plot, PSW samples from SAS2021 fell on binary mixing lines from years 1997 to 2010 of the surface layer
295 input function with global fallout, translating to tracer ages of 11 to 24 years (Fig. 6). Shallow waters (around 30 m depth, thick black outline) from the central Amundsen Basin (stations 16 and 20) were the youngest (11-17 years). They showed the highest tracer concentrations, i.e., the least dilution with the global fallout signal. The shallow waters at station 8 (at the Gakkel Ridge) were slightly older (around 18 years) and more diluted compared to the central Amundsen Basin.

300 As pointed out above (Section 3.2), station 5 in the Nansen Basin had low tracer concentrations, both in I129 and U236, drawing it towards the global fallout end-member. This has been observed earlier (Wefing et al., 2021), and since dilution with Pacific Water is not expected at the surface of Nansen Basin, it is most likely explained by northward-flowing FSBW. This branch carries significantly lower concentrations of I129 and U236 compared to the surface layer input function (NCC,
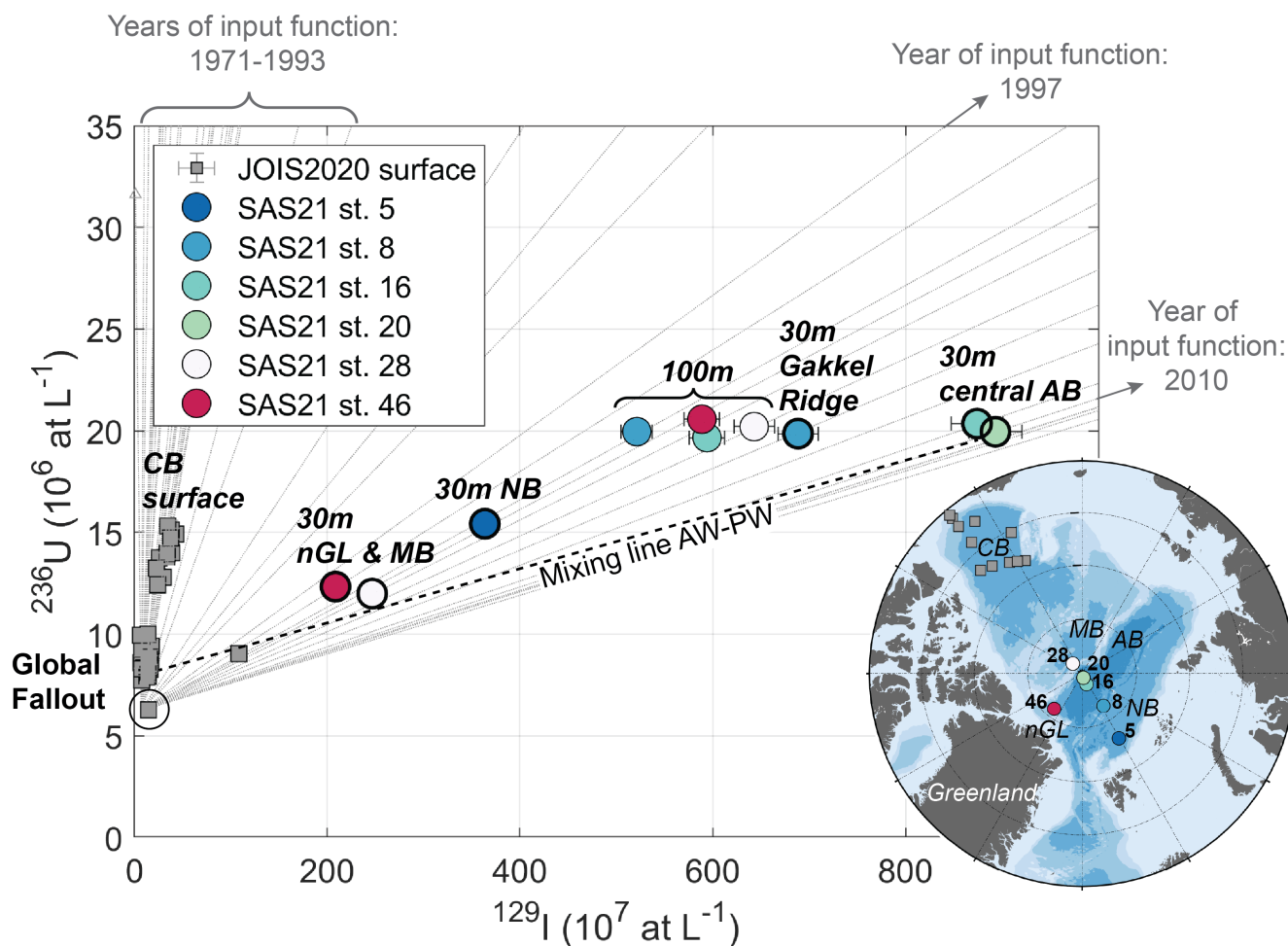
14

Figure 6. Plot of U236 against I129 concentrations with binary mixing lines (in grey) between individual years (1997-2010) of the surface layer input function (Fig. 2) and the global fallout background signal. SAS2021 PSW samples are color-coded by station. Thick black outline marks samples from around 30 m depth, thin black outline marks samples from around 100 m depth. CB: Canada Basin, nGL: north of Greenland, MB: Makarov Basin, NB: Nansen Basin, AB: Amundsen Basin. Samples from PSW in the Canada Basin collected in 2020 (JOIS2020, Payne et al., 2024) are shown in grey squares.

Casacuberta et al., 2018), which was confirmed again in the recent study by Pérez-Tribouillier et al.. Radionuclide concentra-
305 tions in the Nansen Basin are not well described by the surface layer input function and are excluded from further interpretation.

Note the much higher tracer ages (30-50 years) and higher dilution of the tracer signal in PSW samples from the Canada
Basin (JOIS2020, grey squares in Fig. 6) compared to the SAS2021 samples from the central Arctic. This is due to the longer
travel time of Atlantic Water to the Canada Basin and mainly Pacific Water being present at the surface (see also Payne et al.,
310 2024).

4.1.2 Pacific water extent

Pacific water carries a low I129 and U236 tracer signal, corresponding to global fallout (latest estimate by Payne et al. (2024)).
In order to assess the presence of Pacific water in the study area based on the tracer distribution, however, other tracer-free
315 water masses have to be considered, here meteoric water (mainly river water) and sea-ice meltwater.

The overall decrease of I129 (and U236) with decreasing salinity throughout the PML in Section 1 (Fig. 5c and Fig A1)
points to a dilution of the tracer signal with low-salinity water. The combination of salinity, stable oxygen isotopes (δ^{18}O),
and N:P fractions was used to calculate meteoric, sea-ice meltwater, Atlantic and Pacific Water fractions (e.g., Östlund and
320 Hut, 1984; Bauch et al., 2011; Paffrath et al., 2021), here using end-member values from Bauch et al. (2011) and following
the calculations outlined therein (Fig. A2a-c). Meteoric water fractions were up to 12 %% (highest at the surface). In contrast,
sea-ice meltwater fractions were mostly negative (between -4 and 0 %%), pointing to net sea-ice formation, and highest for the
stations north of Greenland (up to 2 %%).

325 Assuming negligible to no I129 input by meteoric water (Casacuberta et al., 2016), I129 concentrations were corrected to
100 %% saline water by the calculated meteoric water fractions (Fig. A2d, sea-ice melt was omitted since it was largely negative
or around zero). Also, after correcting for the meteoric water fraction we still observed a decrease in I129 towards the surface,
which showed that dilution with meteoric water only explains part of the decrease in I129 towards low salinities. Therefore,
dilution with Pacific Water likely explains the decrease of I129 concentrations towards the surface. Pacific Water fractions
330 obtained from N:P ratios are debated and have large uncertainties (e.g., Alkire et al., 2015, 2019; Whitmore et al., 2020), how-
ever, they still serve for an overview of the spatial distribution of Pacific Waters across the sampling area. For the SAS2021
samples, N:P based Pacific Water fractions suggest that Pacific Water was present in all PSW samples, with highest fractions
found in the Makarov Basin (Fig. A2c), supporting the hypothesis of tracer dilution by Pacific Water at all stations. This is also
corroborated by the dual-tracer plot (Fig. 6), where samples from north of Greenland and the Makarov Basin fell on a mixing
335 line between the central Amundsen Basin samples to Canada Basin surface samples close to global fallout. Note that from the
N:P ratio method, we obtained similar Pacific Water fractions for PSW in the Amundsen Basin and north of Greenland. At the
same time, I129 concentrations are significantly different between both regions. This might be caused by an overestimation

of N:P-based Pacific Water fractions for the Amundsen Basin (Alkire et al., 2015; Bauch et al., 2011; Newton et al., 2013), similar to the findings of Alkire et al. (2019) who reported a larger extent of Pacific Water towards the Eurasian Basin based
340 on N:P ratios compared to the NO parameter.

Generally, based on the combined I129 and U236 data, we can hence conclude that the front between Atlantic and Pacific-derived waters in the surface layer of the central Arctic was located somewhere between station 20 and station 28 in 2021, due to the different location of surface samples from these two stations in the U236-I129 mixing plot (Fig. 6). With the better spatial
345 resolution for I129, and the sharp decrease in surface I129 concentration between station 26 (on top of the Lomonosov Ridge) and station 28 (Makarov Basin) (Fig. 3 and Fig. 5), we can restrict it further to the Makarov Basin side of the Lomonosov Ridge. However, the presence of some Pacific Water is required to explain the decrease in I129 in the surface waters of stations 25 and 26, which is supported by N:P ratios.

350 ### 4.1.3   Provenance of Halocline Waters

For the halocline layer, combined I129 and U236 data was available for four stations, two in the Amundsen Basin, one in the Makarov Basin, and one north of Greenland (Fig. 5 and 6, data points from 100 m depth with thin black outline). These data points all plotted at a similar location in the mixing plot, and especially U236 concentrations were strikingly consistent among them. Note that these samples also had the highest I129 concentrations throughout the water column in the Makarov Basin and
355 north of Greenland (Fig. 3).

Based on their T and S properties, the two samples from the Amundsen Basin (station 8 and 16) were associated with the LHC, which is formed north of the Barents Sea from cooled and freshened Atlantic Water carried in Fram Strait and Barents Sea Branch Water, and through the addition of low-salinity shelf water mainly from the Laptev Sea (Rudels et al., 1996). The
360 samples from the Makarov Basin (station 28) and north of Greenland (station 46) had practical salinities slightly below 34. They were, therefore, classified as UHC waters by hydrographic properties and are thought to be derived from Pacific inflow but also influenced by the East Siberian Sea (e.g., Anderson et al., 2017). However, this is not supported by the radionuclide concentrations. The similar location of the 100 m samples from the different stations in the dual-tracer plot suggests a common origin or formation region and transport route for these halocline waters, before they are transported across the Arctic
365 Ocean towards Greenland. This is also supported by the additional available I129 data, where samples from the Amundsen and Makarov Basins showed similar I129 concentrations throughout the LHC layer (Fig. 5c and Fig. A5a). Furthermore, the comparably high tracer concentrations suggest only little Pacific-origin water but a significant fraction of tracer-labeled NCC-origin waters, which are transported along the Eurasian shelf and contribute to the formation of halocline waters along their way. Based on the I129 and U236 concentrations presented in this study, we conclude that halocline waters formed from Atlantic-
370 origin waters are present throughout the entire study area, including the Makarov Basin and the area north of Greenland. This is also supported by the distribution of the NO parameter at a practical salinity of 34 (NO = $(9 \times NO_3^-) + O_2$, Broecker (1974),

17

Fig. A5b), which does not show a lot of variation across the study area. NO values are below $400\ \mathrm{mmol}\ \mathrm{m}^{-3}$ which was used by Alkire et al. (2019) to discriminate Atlantic from Pacific waters.

4.1.4 Transport Times and Mixing in the Atlantic Layer

For samples from the mid-depth Atlantic Layer and below, the dual-tracer method was only used to infer information on mixing and water mass provenance, since circulation times were obtained from the TTD approach. Lower I129 concentrations, paired with higher U236 concentrations observed in Section 2 compared to Section 1, (Fig. A3) indicate the influence of water from the Canada Basin. AAW samples from Section 2, especially from station 46 north of Greenland, plotted on a mixing line between AAW from Section 1 and AAW from the Canada Basin (JOIS2020, Payne et al., 2024). This suggests that AAW north of Greenland represents a mixture of Atlantic Water that has circulated through the "long loop" (Canada Basin) and the "short loop" (Eurasian Basin), which will be investigated further under the framework of the TTD model.

The TTD method was applied to samples not classified as PSW and down to 1000 m. Deeper samples (1500 m and below) showed U236 concentrations close to the global fallout level or below (Fig. 3), and hence they did not carry significant amounts of the transient reprocessing plants tracer signal. The $\Delta - \Gamma$ grid for the determination of both TTD parameters according to "Smith's method" (see Raimondi et al. (2024) for detailed explanation) is shown in the appendix (Fig. A4).
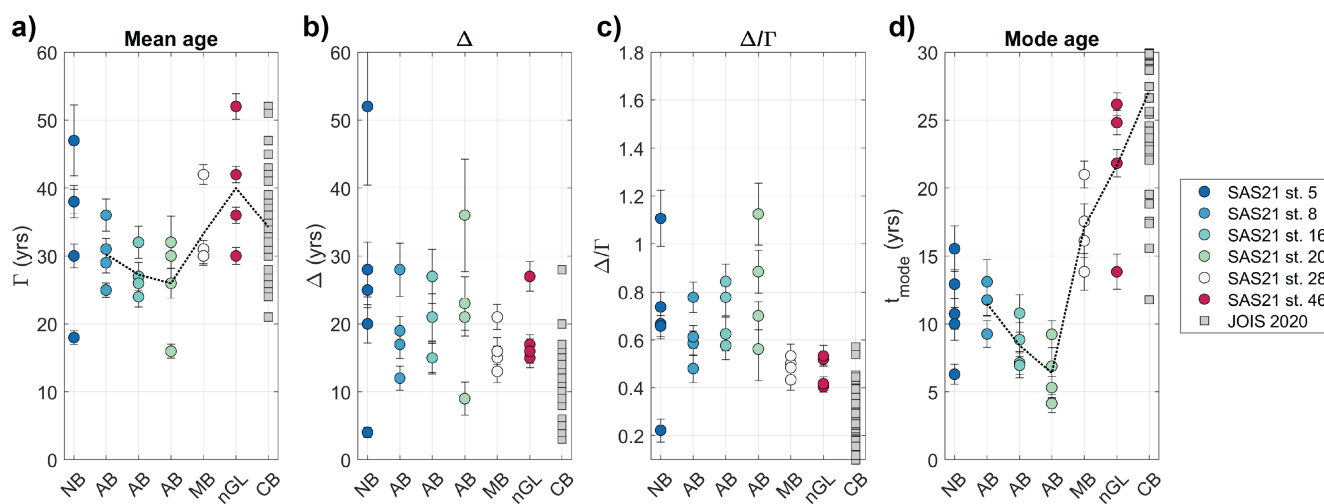

Figure 7. TTD parameters Γ (mean age, a), Δ (b), derived Δ/Γ ratio (c), and derived t_{mode} (mode age, d) plotted against different Arctic Basins for Atlantic layer samples from SAS2021 (down to 1000 m depth), color-coded by station. NB: Nansen Basin, AB: Amundsen Basin, MB: Makarov Basin, nGL: north of Greenland, CB: Canada Basin. Samples from the Atlantic layer in the Canada Basin collected in 2020 (JOIS2020, Payne et al., 2024) are shown in grey. Dashed lines in (a) and (d) connect mean values for each station.

The two parameters of the TTD obtained for the SAS21 samples and the Canada Basin 2020, Γ and Δ, as well as the derived
390   parameters Δ/Γ and the mode age t_{mode}, are plotted in Fig. 7. Different stations from SAS2021 are color-coded and sorted by
basin. For SAS2021, mean ages were overall in the range of 15-55 years, Δ largely between 9-40 years, Δ/Γ ratios were in
the range of 0.4-1.2, and mode ages were below 30 years. Δ/Γ ratios were generally higher in the Amundsen Basin (between
0.4 and 1.2) compared to the Makarov Basin and north of Greenland (both between 0.4 and 0.6). Confirming previous studies
(Wefing et al., 2021; Raimondi et al., 2024), Δ/Γ ratios were lower in the Canada Basin than in all other basins. Note the
395   large spread in Γ and Δ for the Nansen basin (station 5). Since this station is not located downstream of the initialization
point of the Atlantic Layer input function (the St. Anna Trough, where FSBW and BSBW merge), the TTD analysis is not
expected to provide meaningful results. This was already shown in earlier studies (Wefing et al., 2021; Raimondi et al., 2024;
Pérez-Tribouillier et al.) and we will not include the samples from station 5 in the further interpretation.

400   Mean and mode ages both decreased from the Gakkel Ridge (station 8) towards the Lomonosov Ridge (station 20, Fig. 7a
and d). From there, both ages increased towards the Makarov Basin and north of Greenland. Both trends were more pronounced
in the mode age compared to the mean age, especially the abrupt change in the mode age when crossing the Lomonosov Ridge
(from station 20 to 28). Previous studies suggested the mode age as a more suitable age measure for the lateral transport of
Atlantic Water in the Arctic Ocean compared to the mean age (Smith et al., 2011; Wefing et al., 2021). The decrease in mode
405   ages from the central Eurasian Basin towards the Lomonosov Ridge suggests that waters in the mid-depth Atlantic layer are
transported faster close to the ridge, which could be explained by transport in a branch of the Arctic Ocean Boundary Current
flowing along the Amundsen Basin side of the Lomonosov Ridge. The same spatial pattern was observed by Körtke et al.
(2024), investigating tracer ages from CFC-12 and SF_6, as well as Pasqualini et al. (2024), from ^{3}H-^{3}He ages. However, in-
terestingly, Δ/Γ ratios do not suggest very advective transport at station 20, but rather increase from the interior Eurasian
410   Basin towards the Lomonosov Ridge, pointing to more mixing along the flow. In the Makarov Basin, north of Greenland, and
in the Canada Basin, low Δ/Γ ratios and high mode ages point to more advective flow, but a longer pathway of waters. The
significantly higher mode ages in the Makarov Basin suggest that waters have been transported along a different (longer) loop
compared to the Amundsen Basin. A difference in water mass ages between both sides of the Lomonosov Ridge was also
observed by Tanhua et al. (2009) and Gerke et al. (2024), albeit in mean ages derived from gas tracers. Both studies found
415   higher mean ages, i.e., a slower ventilation, in the Makarov Basin compared to the Amundsen Basin, with a sharp front over
the Lomonosov Ridge. This is in line with our findings based on I129 and U236, confirming that anthropogenic radionuclides
and gas tracers such as CFCs and SF_6 act as similar Atlantic Water tracers in the Arctic Ocean once the Atlantic Water layer is
isolated from atmospheric gas exchange. This has also been discussed in Raimondi et al. (2024), with implications for anthro-
pogenic carbon estimates from I129 and U236.

420

As mentioned above, tracer concentrations at station 46, located north of Greenland, pointed to a mixture of Atlantic Wa-
ter coming from the Canada Basin and the Amundsen Basin. This is also reflected in the PDFs constructed for the available
samples from this station. Compared to the PDFs from the Canada and Amundsen Basins, PDFs at station 46 had a large
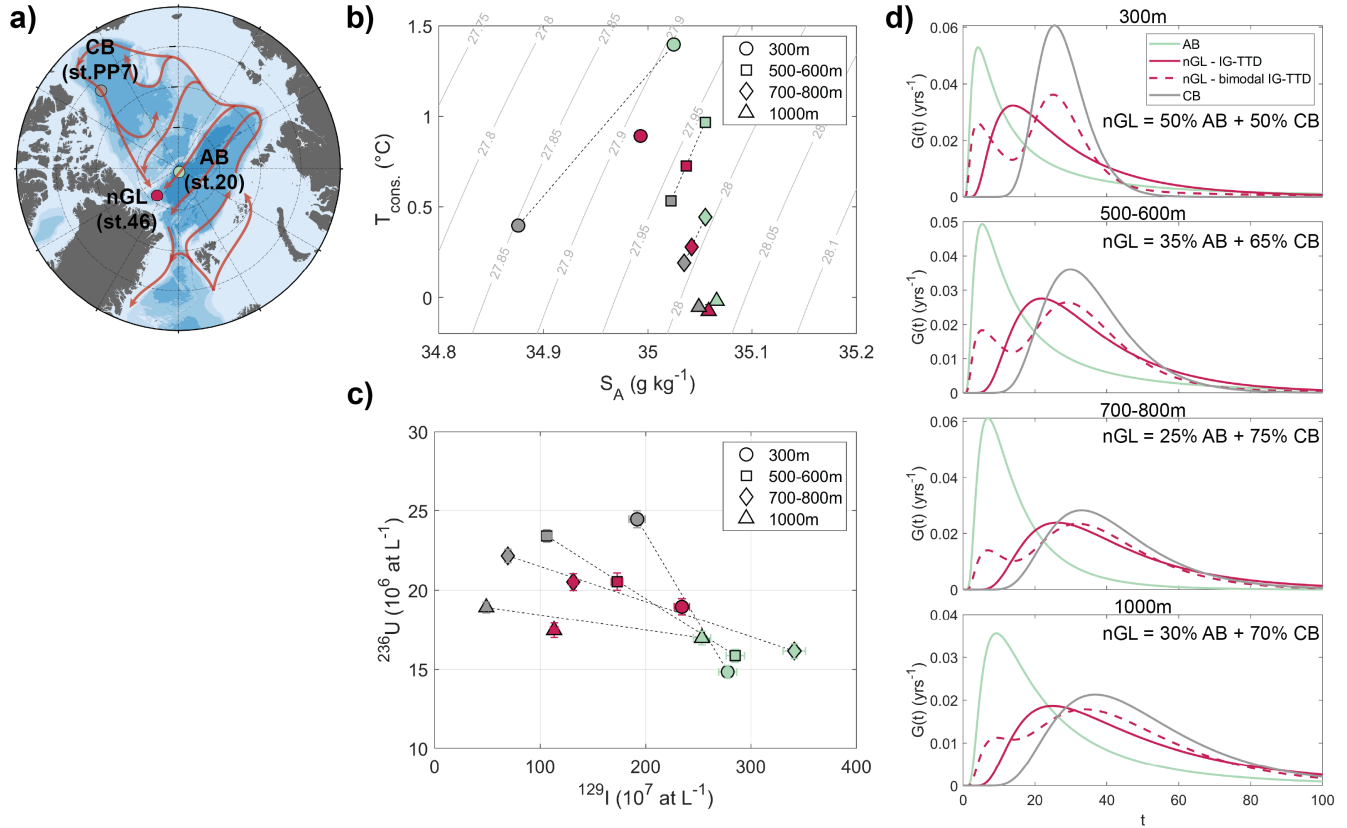
19

Figure 8. (a) Map showing station PP7 in the Canada Basin (CB), 20 in the Amundsen Basin (AB) and 46 north of Greenland (nGL). Red arrows depict suggested Atlantic Water circulation, where station 46 is a mixture of waters from the other two stations. (b) T-S plot (conservative temperature against absolute salinity) of samples from available depths (300-1000 m, different symbols) from all three stations (color-coded). (c) U236-I129 plot of samples from available depths (different symbols) from all three stations (color-coded). (d) PDFs G(t) for available depths, color-coded by station. Dashed line depicts the bimodal IG-TTD for station 46.

width (large Δ) and hence a lower maximum probability, indicating the presence of more different ages within the distribution.
In fact, the mixture of two branches with a different transport history is not captured by the TTD model using a unimodal inverse Gaussian function. Instead, Smith et al. (2022) described the linear combination of two inverse Gaussian functions, each defining the flow field in the respective branch. We assumed that Atlantic Water from each available sampling depth at station 46 can be described as a mixture of waters from similar depth at station PP7 in the Canada Basin (Fig. 8a and Payne et al. (2024)) and station 20 in the Amundsen Basin. This is corroborated both by a T-S plot (Fig. 8b), as well as a U236-I129 plot (Fig. 8c), where dotted lines indicate linear mixing of CB and AB waters from respective depths. Note how samples from station 46 (dark red) plotted close to or directly on the mixing lines even though the sampling depths/potential density of the available samples did not match exactly. Based on the mixing lines in U236-I129 tracer space, we calculated fractions of

Amundsen Basin water found at each depth of station 46, and from those, the bimodal IG-TTD from the individual TTDs of
the end-members assuming a linear combination of two IG-TTDs (see equation 4). The resulting bimodal TTDs for station 46
435 are shown in Fig. 8d (dark red, dashed), along with the unimodal IG-TTDs of both end-members and station 46 (dark red,
continuous). The mean age of the bimodal TTDs is a linear combination of the mean ages of both end-members. Mean ages
derived for station 46 from the bimodal TTD were lower compared to those from the unimodal TTD for all depths except
300 m. This result is more reasonable given that the unimodal mean ages were on the order of or even exceeding those from
the Canada Basin (see also Fig. 7a). The effect is also seen in the more rapid decrease of the bimodal TTD at old ages (Fig. 8d).
440 Δs do not mix conservatively, but are always higher in the mixture compared to a linear combination of the two end-members
(see, e.g., Fig. 2b in Smith et al., 2022). For the sample from around 700 m depth, the Δ corresponding to the bimodal TTD
even exceeded the individual Δs of the end-members. In general, however, compared to the unimodal TTD for station 46, the
Δ of the mixture was higher for the upper two samples and lower for the others. When the flow field is described by a bimodal
TTD, a single mode age cannot be attributed. Instead, the ages with the local maxima in the PDF describe the influence of the
445 two end-members. Note that for station 46, the overall highest probability in the PDF was associated with the Canada Basin
branch for all depths. Overall, we conclude that the Atlantic Water transport north of Greenland should rather be described by
a bimodal TTD than a unimodal one, considering the two branches of Atlantic Water being advected from the Amundsen and
Canada Basins. This applies to other regions of the Arctic Ocean as well, such as the mixing of Atlantic and Pacific-derived
water over the Chukchi Sea shelf described in Smith et al. (2022).

450

4.2 Temporal changes in Atlantic Water circulation between 2011 and 2021

4.2.1 Changes in Polar Surface Water

To assess temporal changes in Polar Surface Waters, we compared available I129 data collected in the Eurasian and Makarov
Basin between 2011 and 2021 (see Table 1). The distribution of I129 concentrations in the surface (around 10-30 m depth
455 depending on sample availability) showed the overall pattern of a higher I129 tracer signal in the Eurasian (especially the
Amundsen) Basin, and lower I129 concentrations in the Makarov Basin and north of Greenland (Fig. 9a). While the surface
Makarov Basin (close to the North Pole) appeared to be dominated by Pacific Water in 2021, one station (station 10) suggested
a stronger Atlantic Water signal in this region in 2012. A similar trend was observed further upstream. Station 245 indicated a
stronger Atlantic Water signal in 2011, while station 134 showed a lower tracer concentration and hence less Atlantic Water at
460 a similar location in 2015 (see also Wefing et al. (2021) for further discussion).

Atlantic and Pacific Water fractions for the same datasets were also calculated based on the N:P method, again following
the method by Bauch et al. (2011, see also Section 4.1.2), albeit using a three-end-member model of Atlantic, Pacific, and
freshwater due to limited availability of δ^{18}O data (calculations outlined in Appendix B). Atlantic Water fractions in the sur-
465 face were limited to the Eurasian side of the Lomonosov Ridge in 2015 and 2021 (Fig. 9b). In 2011, however, high Atlantic
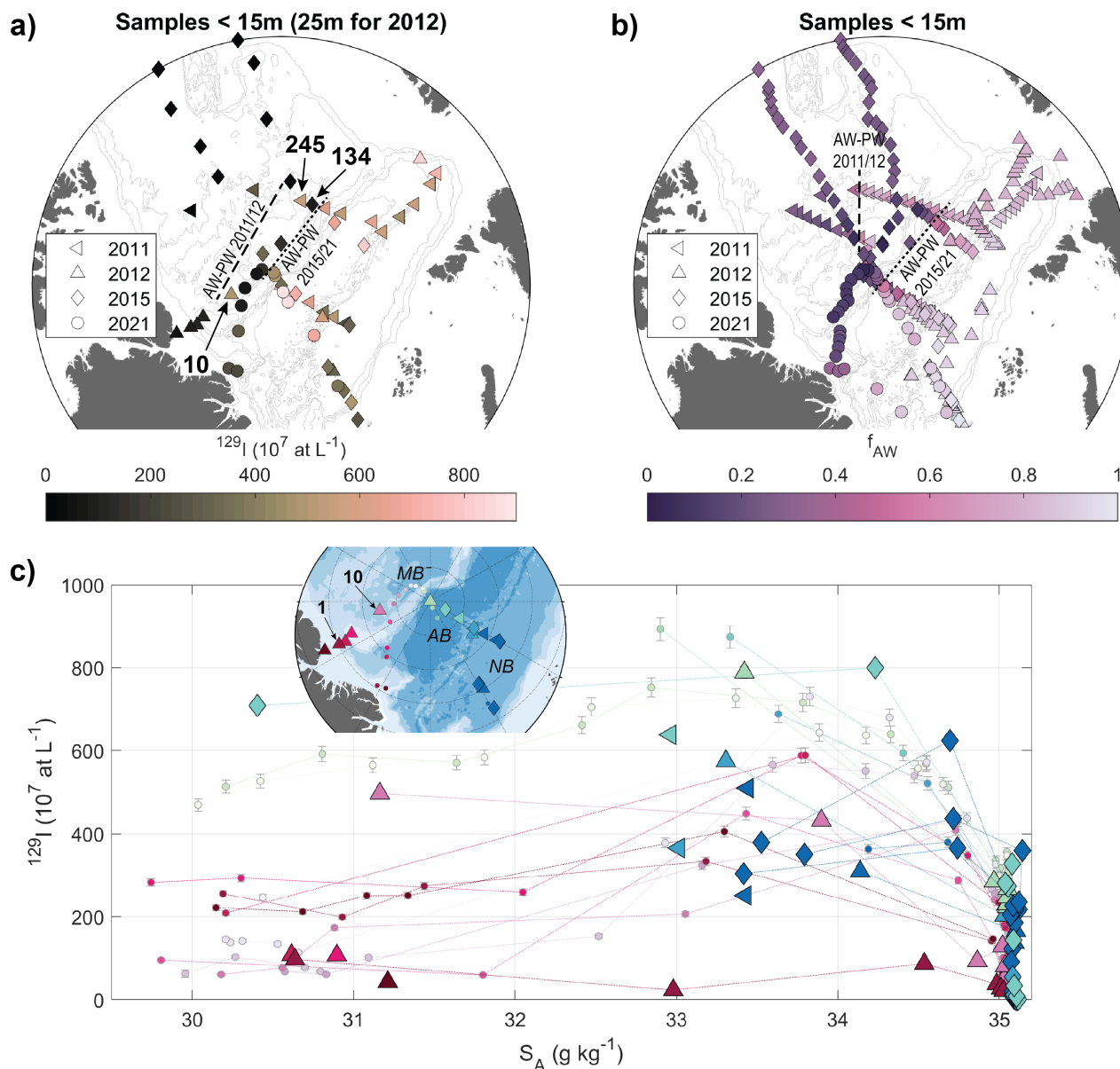
Figure 9. (a) Isosurface map of I129 concentrations in the surface (< 15 m depth for 2011, 2015, 2021; 25 m depth for 2012 due to sampling depth resolution). The front between Atlantic- and Pacific-derived surface waters based on I129 concentration for 2011/12 is indicated by a dashed line, and for 2015/21 by a dotted line. (b) Isosurface map of Atlantic Water fractions (f_{AM}) derived from salinity and N:P fractions, for all available data from the surface layer from the same expeditions as in (a). The front between Atlantic- and Pacific-derived surface waters based on N:P ratios for 2011/12 is indicated by a dashed line, and for 2015/21 by a dotted line. (c) Plot of I129 concentration against absolute salinity for available stations from 2011, 2012, 2015, 2021. Note that 2021 data is the same as in Fig. 5c. Stations are color-coded by region, following color-coding for SAS2021 stations.

Water fractions were observed in the Makarov Basin, extending to the Alpha-Mendeleyev Ridge, which is in line with the I129 distribution.

470   It should be noted that the sampling resolution for I129 was sparse, especially in the earlier years and often limited to "surface samples", with depths varying between 5 and 30 m. The high-resolution I129 sampling in the upper 50 m at several SAS2021 stations showed significant variation in the I129 concentration in this highly dynamic layer (Fig. 3a, c and 5c). To take varying sampling depths and changes in the water mass composition into account, all samples collected in the vicinity of the SAS2021 stations in different years were added to the SAS2021 I129-Salinity plot (Fig. 9c). The available depth profile from the Lincoln Sea from 2012 (station 1), upstream of the SAS2021 stations north of Greenland, clearly reflected Canada

475   Basin waters carrying very low I129 concentrations across the entire Polar Surface Water layer (and below). In contrast, the higher I129 concentrations observed in the SAS2021 stations located further downstream, north of Greenland (dark red circles), pointed to a significantly higher fraction of Atlantic-origin water being transported to this region in 2021, presumably from the Amundsen Basin. As also seen in the isosurface map (Fig. 9a), station 10 from 2012 showed higher I129 concentrations compared to 2021 samples from nearby stations and corresponding salinities. I129 concentrations observed at this location in

480   the Makarov Basin in 2012 almost matched those observed on top of the Lomonosov Ridge, close to the North Pole, in 2021 (light green circles).

In summary, both the distribution of I129 and N:P-based Atlantic Water fractions, suggested Atlantic-origin water reaching further across the Lomonosov Ridge and into the Makarov Basin in 2011 and 2012, compared to the years 2015 and 2021,

485   implying a change in the surface water circulation. Temporal changes in the Atlantic-Pacific Water front have been investigated in earlier studies, using both, nutrient relationships (e.g., Alkire et al., 2007, 2015) and I129 (Karcher et al., 2012; Smith et al., 2021). They have generally been found to be associated with different states of atmospheric circulation patterns and coupled oceanic responses, described by indices such as the Arctic Oscillation (AO; e.g., Morison et al., 2012), the Arctic Ocean Oscillation (AOO; e.g., Proshutinsky et al., 2015), or the Arctic Dipole (AD; e.g., Polyakov et al., 2023).

490

Smith et al. (2021) found that changes in the surface I129 distribution across the Arctic Ocean reflect a change from a cyclonic circulation mode associated with a positive AO index in the mid-1990s to an anti-cyclonic circulation mode along with a negative AO index in the 2000s. This change was accompanied by a shift in the Atlantic-Pacific Water front from the Alpha-Mendeleyev Ridge (1990s) to the Lomonosov Ridge (2015). Our analysis of I129 concentrations between 2011 and

495   2021 indicated that this shift was still ongoing between 2011 and 2015, but the position of the front did not change further between 2015 and 2021. Polyakov et al. (2023) described an increasingly positive phase of the Arctic Dipole (AD+) between 2007 and 2021, leading not only to enhanced inflows of Atlantic Water through the Barents Sea Opening compared to Fram Strait, but also to a shift in the alignment of the Transpolar Drift from the Amerasian Basin towards the Lomonosov Ridge. This is again supported by the change in surface I129 distribution, where the available tracer data suggests that a strong shift

500 occurred between 2011 and 2015.
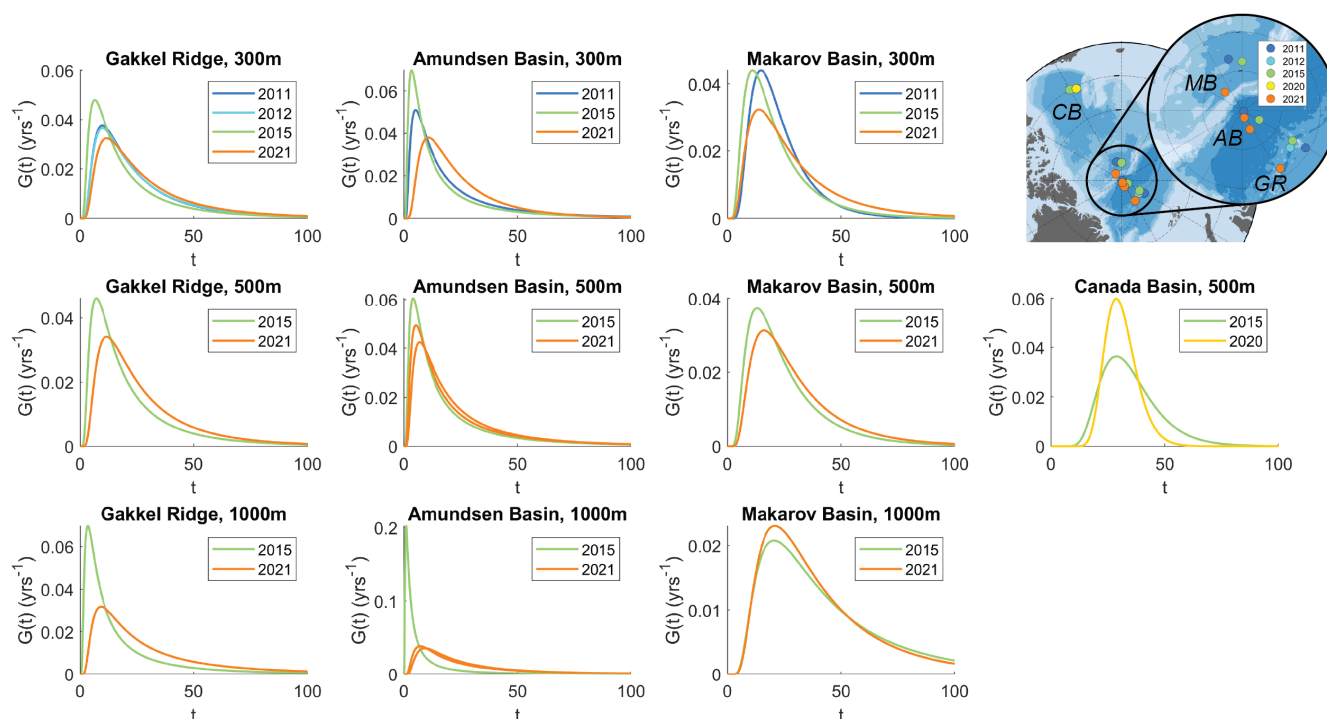
4.2.2 Changes in the Atlantic Layer and below

Figure 10. PDFs G(t) for matching stations from different sampling years (2011 - 2021). Rows are different depths (300, 500, 1000 m), columns are different regions/basins. Stations and regions are shown in the map. GR: Gakkel Ridge, AB: Amundsen Basin, MB: Makarov Basin, CB: Canada Basin. TTD parameters can be found in Appendix C.

For the Atlantic Layer, we focused on temporal changes in circulation times and transport characteristics. PDFs were obtained from the TTD model with I129 and U236 for available stations within different Arctic regions, spanning the years 2011
505 to 2021 (Fig. 10, see Table 1 for details on available tracer data). PDFs from different years were compared at different depth layers where most samples were available (300, 500, 1000 m). Note different scales for G(t).

For the Eurasian Basin (stations at Gakkel Ridge and Amundsen Basin), the PDFs showed an increase of mean and mode ages over time, especially from 2015 to 2021. Δ did not show a clear trend and was largely similar in all years (Fig. A6). These
510 findings suggest a slowdown in the circulation of Atlantic Water to the Amundsen Basin between 2015 and 2021 that was not accompanied by an increase in mixing along the flow path.

PDFs from the Makarov Basin showed a similar behavior between 2015 and 2021 down to 500 m depth. As for the Amundsen Basin, Δ remained largely unchanged over time. In contrast to the Amundsen Basin, mode ages in the Makarov Basin in
515 2015 and 2021 did not show a clear increasing trend.

In the Canada Basin samples from different years were only available at 500 m depth. While no change in the mode ages was observed, the shape of the PDF was altered due to a decrease in both Γ and Δ from 2015 to 2020 (Fig. A6).

520 Overall, the comparison of TTD parameters from 2015 and 2021 showed little to no changes in mixing within the Atlantic Water transport (TTD parameter Δ) in different locations in the Amundsen Basin, the Makarov Basin close to the Lomonosov Ridge, and a location in the Canada Basin. Mode ages have been shown to be a good measure of lateral circulation times of Atlantic Water (Smith et al., 2011; Wefing et al., 2021; Raimondi et al., 2024) and the observed increase in mode ages in the Amundsen and Canada Basins suggests a slowdown in Atlantic Water circulation between 2015 and 2021.

525

4.2.3   Comparison to temporal variability observed with gas tracers

Changes in Atlantic Water transport and ventilation up to 2021 have also been investigated using gas tracers (Gerke et al., 2024). Their study was based on CFC-12 and SF_6 data from SAS21 as well as from earlier years (1991, 2005, 2015) using the "classical" TTD method (see Raimondi et al. (2024) for differences to our method) and focusing on the obtained mean ages.
530 Overall, Gerke et al. (2024) observed a similar trend to this study, with an increase in mean ages from 2015 to 2021 across the entire Atlantic Water layer in the Amundsen Basin. Since the gas tracers are introduced from exchange with the atmosphere, the increase in mean ages was interpreted as a slowdown in ventilation in 2021 compared to 2015 (and 2005). In the Arctic Ocean, the mid-depth Atlantic Layer is isolated from the atmosphere after subduction in the region of the St. Anna Trough, hence the increase in mean ages obtained from gas tracers can also be interpreted as a measure for Atlantic Water circulation
535 times, similar to the radionuclide tracers (Gerke et al., 2024; Raimondi et al., 2024). Gerke et al. (2024) speculate about a decrease in the strength of the Arctic Ocean Boundary Current, leading to a slowdown in the lateral circulation of Atlantic Water.

Körtke et al. (2024) investigated temporal changes in Atlantic Water pathways based on tracer ages obtained from CFC-12
540 and SF_6. They largely confirmed the different circulation patterns under changing conditions of the Arctic Oscillation (AO) index suggested by Karcher et al. (2012) and Smith et al. (2021). Lower Atlantic Water tracer ages in the mid-1990s were attributed to a strong boundary current connected to a positive AO index. Increased tracer ages in 2005 and 2015 were interpreted as a weakening of the boundary current and coincided with phases of largely negative or mixed AO index (Fig. A7). In addition, tracer age changes are also attributed to changes in the Atlantic Water pathways (see e.g. Fig. 7 in Körtke et al.,
545 2024). Since 2015, the AO index has largely been positive, based on which a decrease in Atlantic Water tracer ages/circulation times could be expected. This is not observed in our study. However, it is unclear how fast circulation in the mid-depth Atlantic

Layer responds to changes in atmospheric conditions and surface layer circulation.

Another reason for changes in mean ages observed both with gas tracers and radionuclides could be circulation changes in
550 the formation region of mid-depths waters, i.e., Fram Strait and the Barents Sea. Polyakov et al. (2023) describe fluctuations in
the inflow of Atlantic Water through the Barents Sea Opening compared to Fram Strait. This would likely affect radionuclide
tracer concentrations introduced into the mid-depth Atlantic layer through different mixing between the different branches
carrying different tracer concentrations (Casacuberta et al., 2018; Pérez-Tribouillier et al.) and gas tracer input functions de-
pending on surface saturation levels (e.g., Raimondi et al., 2021).

555

The mechanism driving the observed increase in Atlantic Water circulation times from 2015 to 2021 remains unclear and
further research is needed in this regard. This could include the simulation of Atlantic Water tracers in circulation models as
done in Karcher et al. (2012); Smith et al. (2021). Also, a longer period of data coverage is probably needed for the mid-
depth layer, since changes happen slower than the surface layer. To better understand the link to atmospheric conditions, data
560 spanning phases of different atmospheric conditions is required, such as the change in AO index from the 1990s to the 2000s.

5   Conclusion and Outlook

In this study, we used the combination of the radionuclides I129 and U236 to assess Atlantic Water pathways, mixing, and
circulation times, as well as the Pacific Water extent in the central Arctic Ocean in 2021 and to study changes in Atlantic Water
circulation between 2011 and 2021.

565

Along the transect of the SAS2021 expedition covering the Nansen, Amundsen, and Makarov Basins, as well as the region
of the Lincoln Sea north of Greenland, we observed a sharp drop in radionuclide concentrations in the surface layer between
the Amundsen and the Makarov Basin, directly at the Lomonosov Ridge. This was attributed to a significant fraction of Pacific
Water on the Makarov Basin side, carrying low radionuclide concentrations, and was qualitatively supported by Pacific water
570 fractions calculated from N:P (nitrate to phosphate) ratios. For the halocline layer, we found similar radionuclide concentra-
tions across the entire transect, pointing to a common formation area and transport route of the halocline waters. Comparably
high tracer concentrations furthermore indicated the presence of Atlantic-origin waters in the halocline, suggesting that these
waters are formed around the Barents Sea where they picked up the tracer signal of the surface layer input function. This
dataset includes the first available I129 and U236 data from the area north of Greenland and in both, the surface layer (ex-
575 cept the halocline) as well as the mid-depth Atlantic layer, tracer concentrations indicated that these waters were a mixture of
Canada Basin and Amundsen Basin waters. In the mid-depth Atlantic layer, the TTD model provided mean ages, mode ages,
and mixing properties for the flow of Atlantic Water through the Arctic Ocean. Confirming earlier studies based on gas tracers
(CFCs and SF$_6$), we found an increase in mean (and mode) ages when crossing the Lomonosov Ridge from the Amundsen into

26

the Makarov Basin, implying a longer transport route.

580

To assess temporal changes over the past decade, we collated all available I129 and U236 data from the Arctic Ocean from earlier studies. In the surface layer, we found a change in the Atlantic-Pacific Water front, which was aligned with the Lomonosov Ridge in 2015 and 2021, but located further in the Makarov Basin in 2011 and 2012. The same pattern was found based on N:P ratios from the same years. One explanation for this change in the Pacific Water extent lies in circulation changes

585 associated with atmospheric circulation patterns, described by indices such as the Arctic Oscillation index or the Arctic Dipole. Smith et al. (2021) describe the shift of the Atlantic-Pacific Water front from the Alpha-Mendeleyev Ridge in the 1990s to the Lomonosov Ridge in 2015 due to changes in the Arctic Oscillation index. Also, the increasingly positive phase of the Arctic Dipole between 2007 and 2021 was associated with a shift in the alignment of the Transpolar Drift from the Amerasian Basin towards the Lomonosov Ridge (Polyakov et al., 2023). Our data supports these findings and indicates that the shift towards

590 the Lomonosov Ridge continued through 2011 and 2012. By 2015, the front had aligned with the Lomonosov Ridge, and was located at a similar location in 2021.

In the mid-depth Atlantic layer, we found an increase in mean and mode ages obtained from the TTD model in the Amundsen Basin from 2015 to 2021. The same trend was observed by Gerke et al. (2024) using the TTD model with CFC-12 and

595 SF_6. This implies either a slowdown in Atlantic Water circulation, which could be attributed to a decrease in the strength of the Arctic Ocean Boundary Current (Gerke et al., 2024), different Atlantic Water pathways (as discussed in Smith et al., 2021; Körtke et al., 2024), or changes in the inflow region of the tracers (such as changes in Fram Strait and Barents Sea Water inflow as a consequence of the Arctic Dipole state, Polyakov et al., 2023). Further research is needed to identify the mechanism behind these changes.

600

The atlantification of the Arctic Ocean is not restricted to the Eurasian Basin anymore, but was recently found to have reached the Makarov Basin (Polyakov et al., 2025), once more confirming that the Arctic Ocean is undergoing drastic changes. How these changes will affect the Arctic system, from the uptake of anthropogenic Carbon to consequences for ecological systems, remains to be investigated. As part of this, understanding and monitoring changes in the Atlantic Water circulation is

605 crucial. Our study not only confirms that the anthropogenic radionuclides I129 and U236 are powerful Atlantic Water tracers but also that the available tracer data set collected during the past decade is of great value and can now be used to assess temporal changes. During the SAS2021 expedition, an effort was made to couple the sampling of different circulation and ventilation tracers. Following the recent study by Raimondi et al. (2024), these different kinds of tracers can be combined in future studies, allowing, for instance, a more comprehensive assessment of anthropogenic Carbon stored in the Arctic Ocean.

610 To this aim, long-term ventilation tracers such as Carbon-14 and Argon-39 should be included and will allow extending such studies to deeper and older water masses.

Data availability. Radionuclide data (I129 and U236) from the SAS-Oden 2021 expedition are available on Zenodo: https://doi.org/10.5281/zenodo.15056897. Hydrographic data from the same expedition are available on PANGAEA: https://doi.org/10.1594/PANGAEA.951266 and https://doi.org/10.1594/PANGAEA.951264 (downloaded 2024-08-23). Biogeochemical bottle data are available on GLODAPv2.2023

615 (Lauvset et al., 2024): https://glodap.info/index.php/merged-and-adjusted-data-product-v2-2023/ (downloaded 2024-06-17).

Appendix A: Additional Figures
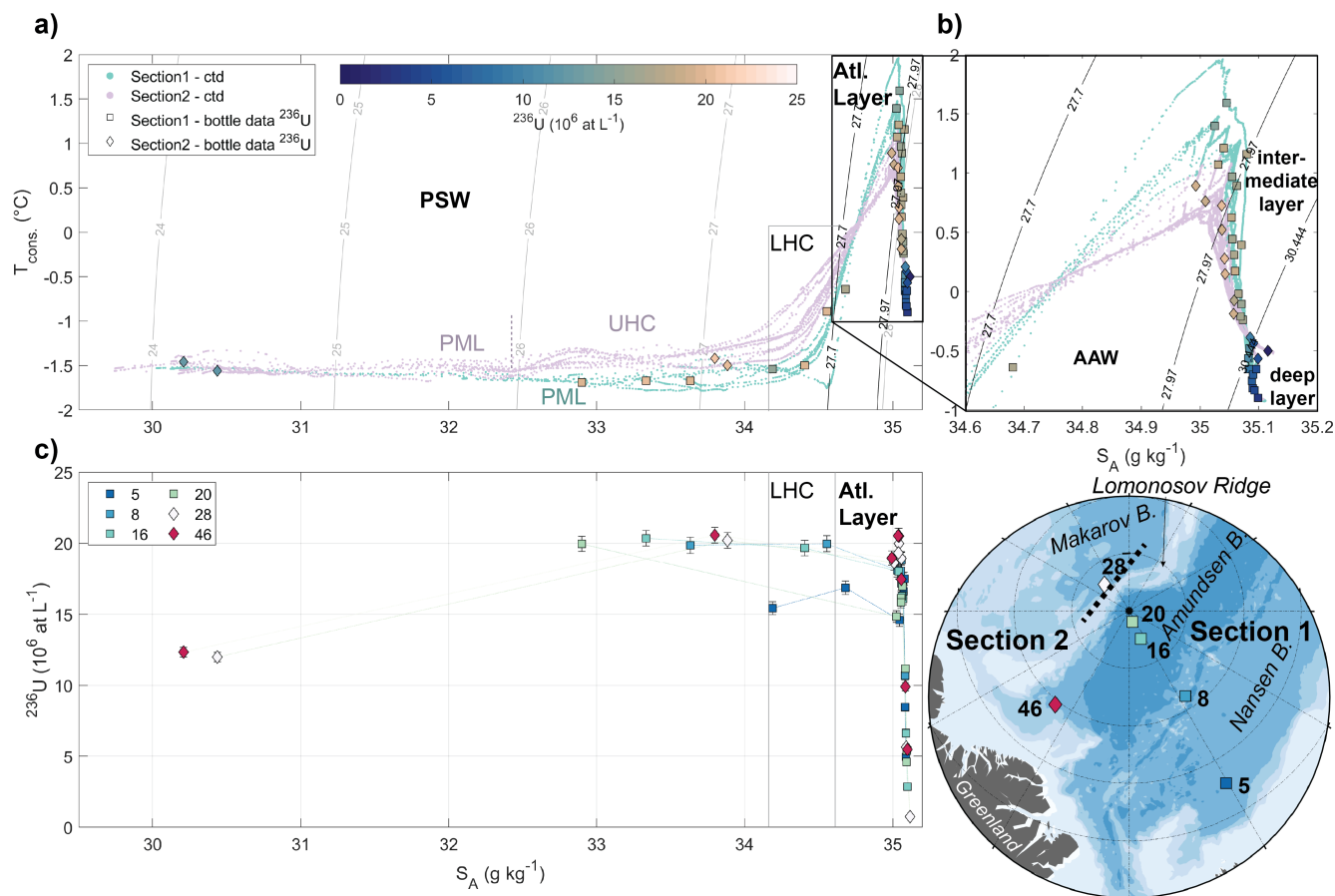
Figure A1. (a) T-S plot (conservative temperature against absolute salinity) with U236 concentrations color-coded and different water masses indicated (PSW: Polar Surface Water, PML: Polar Mixed Layer, UHC: upper halocline, LHC: lower halocline, AAW: Arctic Atlantic Water). Teal and purple dots are 1 m-binned ctd data from Section 1 and 2, respectively. Square and diamond data points are bottle file data from Section 1 and 2, respectively. (b) close-up of the Atlantic Layer (black box in a). (c) Plot of U236 concentration against absolute salinity with stations color-coded.
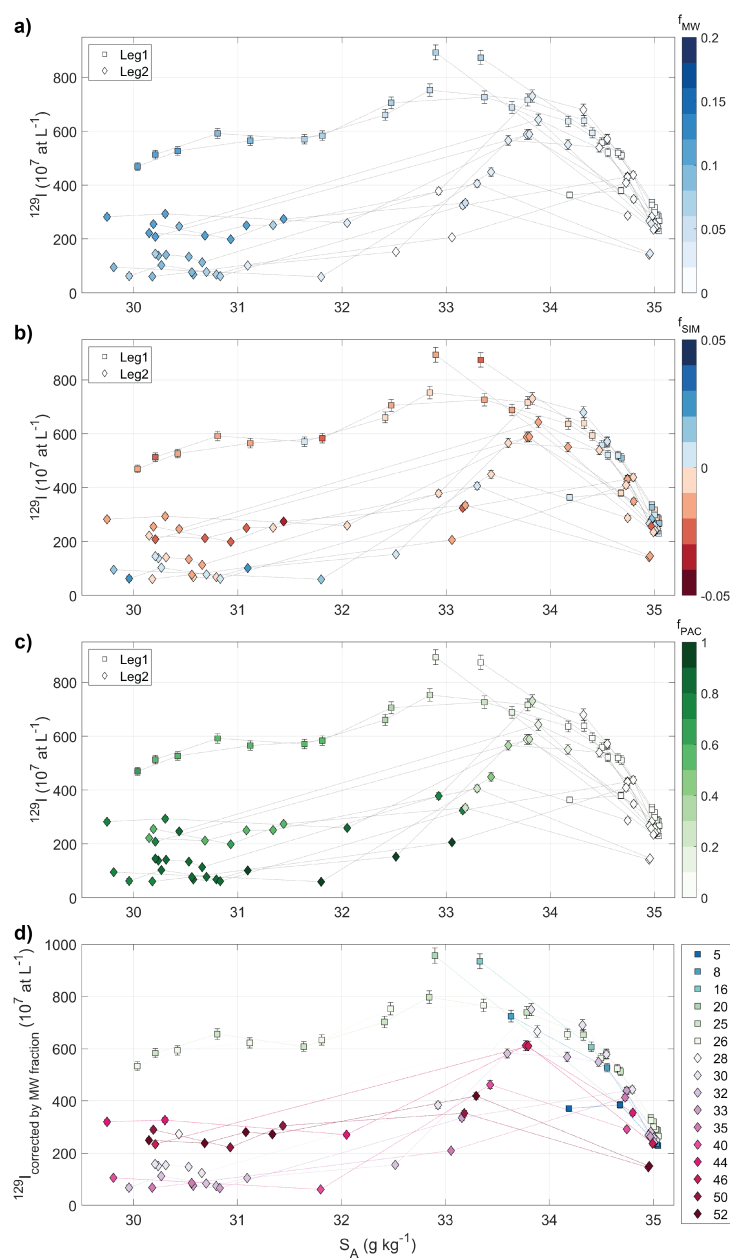
Figure A2. Plot of I129 concentration against absolute salinity with data color-coded by (a) meteoric water fraction f_{MW}, (b) sea-ice meltwater fraction f_{SIM}, (c) Pacific Water fraction f_{PAC}. (d) Plot of I129 concentration corrected by meteoric water fraction f_{MW} against absolute salinity with stations color-coded.
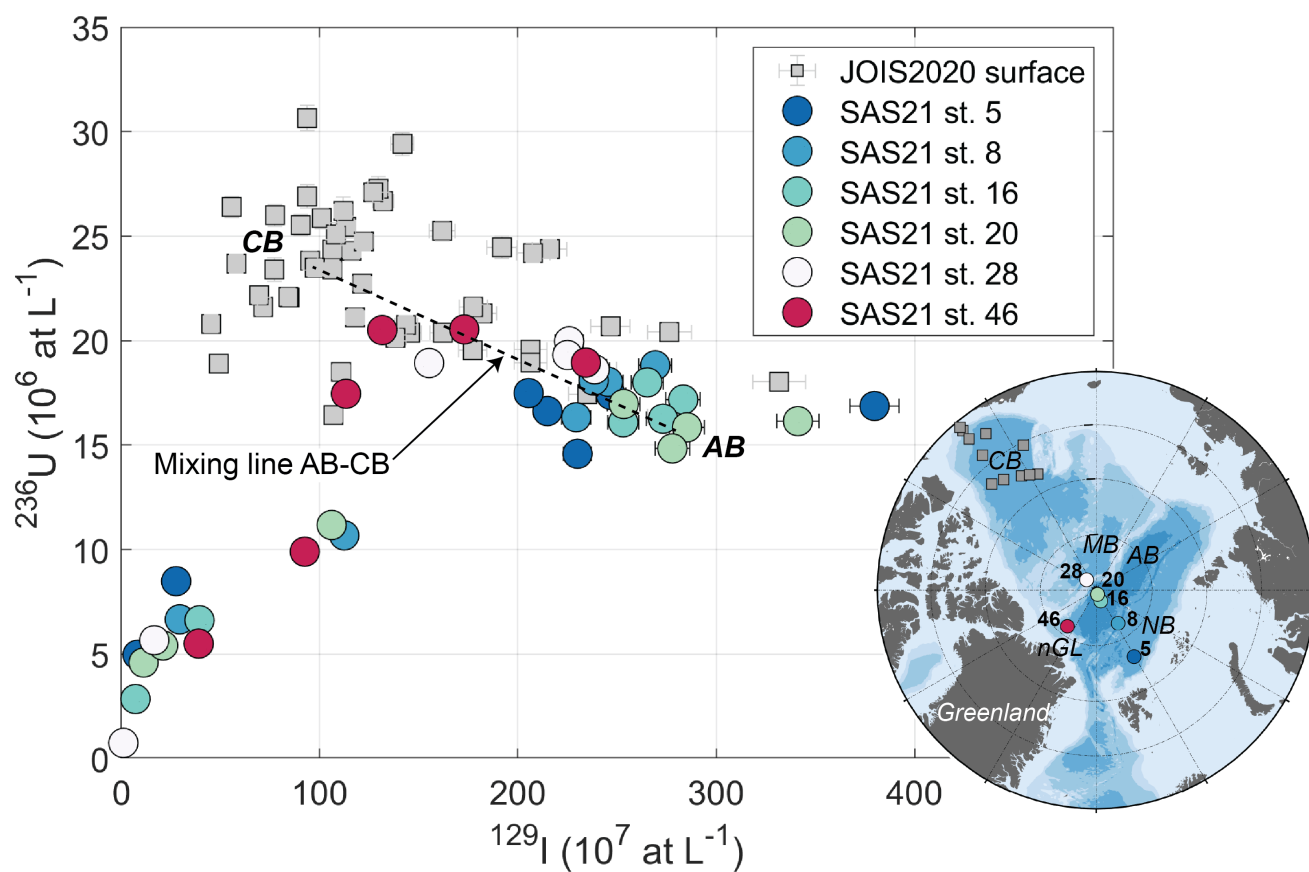
Figure A3. Plot of U236 against I129 concentrations for samples from the Atlantic Layer. SAS2021 PSW samples are color-coded by station. CB: Canada Basin, AB: Amundsen Basin. Samples from the Atlantic Layer in the Canada Basin collected in 2020 (JOIS2020, Payne et al., 2024) are shown in grey squares.
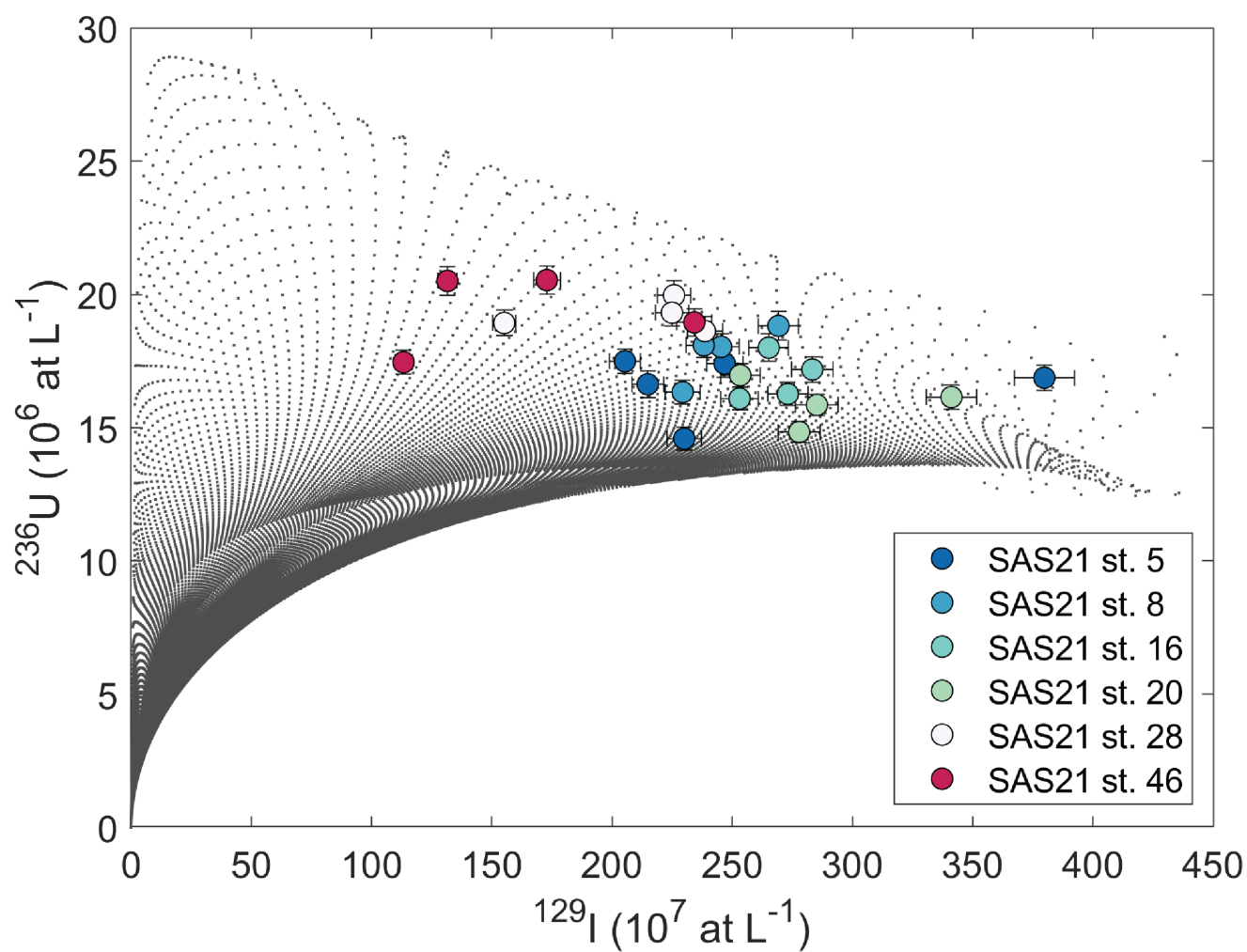
Figure A4. $\Delta - \Gamma$ grid in U236-I129 space for the determination of TTD parameters according to "Smith's method" (see Raimondi et al. (2024) for detailed explanation). SAS2021 samples are plotted on top, color-coded by station.
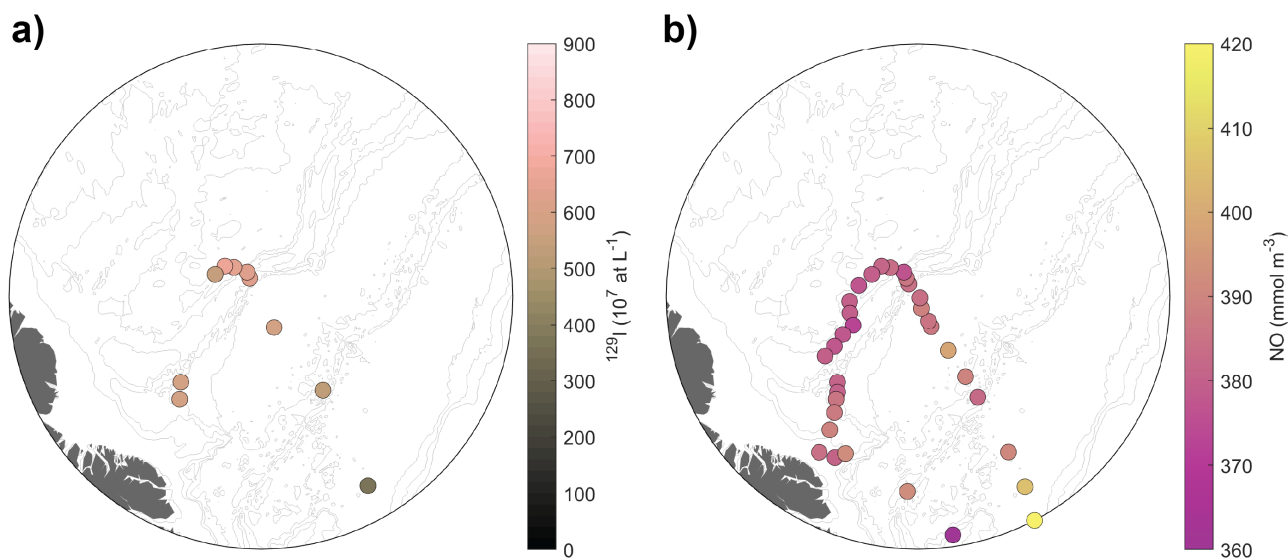
Figure A5. Isosurface maps of (a) I129 concentration and (b) the NO parameter (Broecker, 1974; Alkire et al., 2019) at practical salinity $S_P = 34 \pm 0.5$.
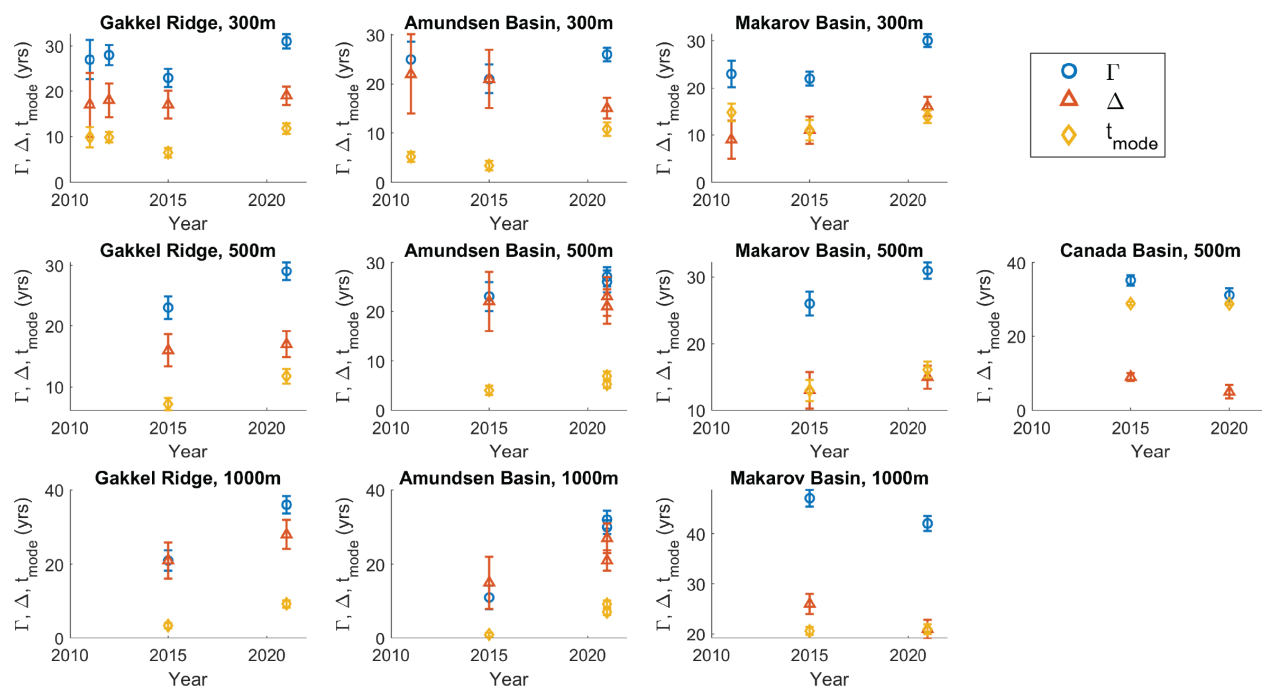
Figure A6. TTD parameters Γ, Δ, and t_{mode} plotted against sampling year. Rows are different depths (300, 500, 1000 m), columns are different regions/basins. Stations and regions are shown in the map in Fig. 10. Data can be found in Appendix C.
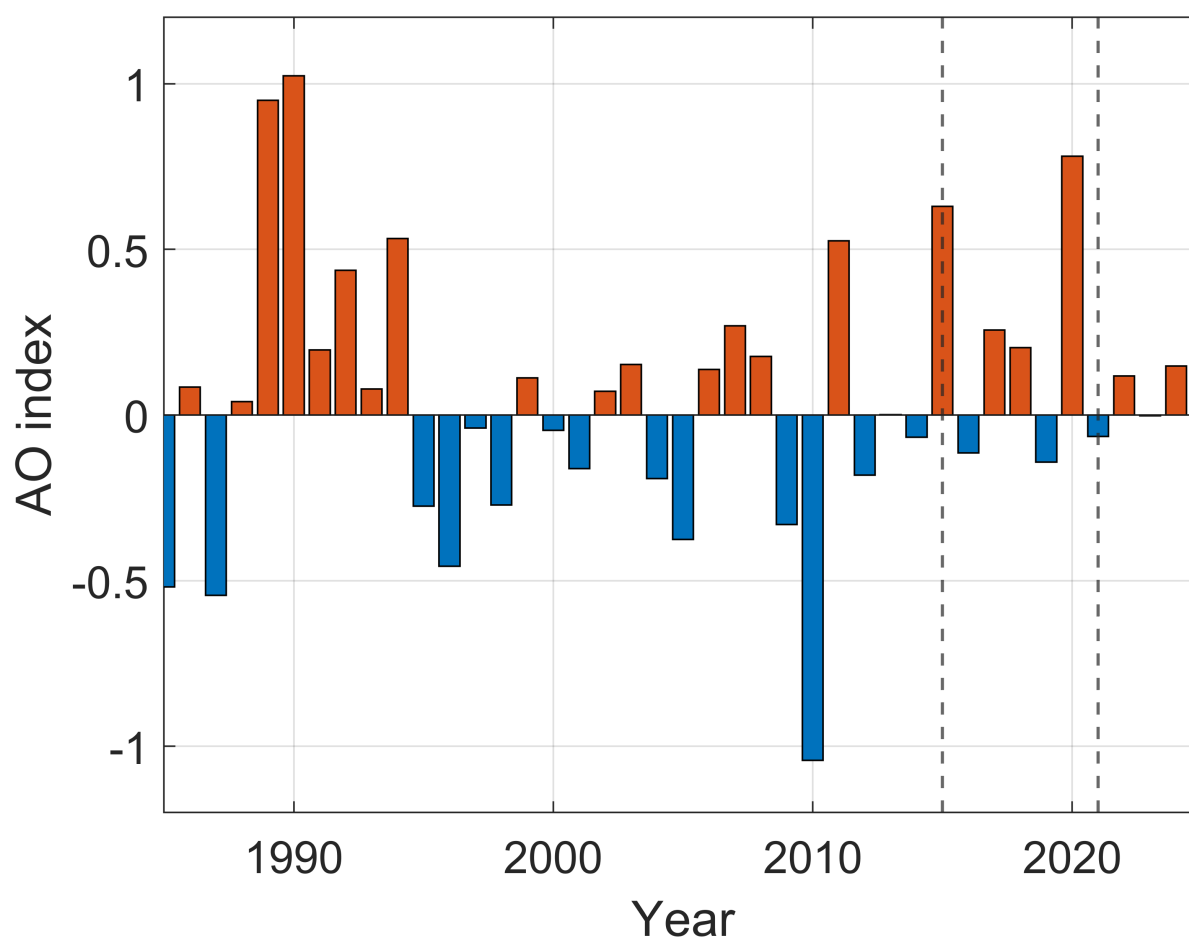
Figure A7. Arctic Oscillation (AO) index (yearly average). Tracer sampling years 2015 and 2021 are indicated as dashed lines. Figure modified after Fig. 6d in Körtke et al. (2024). Arctic Oscillation Data downloaded from: https://www.cpc.ncep.noaa.gov/products/precip/ CWlink/daily_ao_index/ao.shtml (28.02.2025).

Appendix B: Calculation of Atlantic and Pacific Water fractions with three-end-member model

Atlantic and Pacific Water fractions were calculated based on the N:P method, following the method by Bauch et al. (2011), but using a three-end-member model of Atlantic Water (AW), Pacific Water (PW), and freshwater (FW) due to limited availability

620   of $\delta^{18}O$ data. Endmember values were taken from Bauch et al. (2011), for the freshwater endmember we used the river water endmember therein. The three-component mass balance is the following:

$$f_{AW} + f_{PW} + f_{FW} = 1 \tag{B1}$$

$$f_{AW}S_{AW} + f_{PW}S_{PW} + f_{FW}S_{FW} = S_{meas} \tag{B2}$$

$$f_{AW}P_{AW} + f_{PW}P_{PW} + f_{FW}P_{FW} = P_{meas} \tag{B3}$$

625   with $S_{AW} = 34.92$, $S_{PW} = 32.7$, $S_{FW} = 0$, $P_{AW} = 0.0596 \cdot N_{meas} + 0.1139$, $P_{PW} = 0.0653 \cdot N_{meas} + 0.9400$, $P_{FW} = 0.1$.

Hydrographic and nutrient data for expeditions PS78 (2011), PS80 (2012), and PS94 (2015) can be found on PANGAEA: https://doi.org/10.1594/PANGAEA.832164, https://doi.org/10.1594/PANGAEA.774181, https://doi.org/10.1594/PANGAEA. 834081, https://doi.org/10.1594/PANGAEA.819452, https://doi.org/10.1594/PANGAEA.868396, https://doi.org/10.1594/PANGAEA.

630   859559. Hydrographic and nutrient data for expedition HLY1502 (2015) was taken from the GEOTRACES Intermediate Data Product: https://doi.org/10.5285/cf2d9ba9-d51d-3b7c-e053-8486abc0f5fd.

Appendix C: TTD temporal results

Tables with TTD parameters Γ, Δ, and t_{mode} for the different regions/basins, depths (300, 500, 1000 m), and sampling years shown in Fig. A6.

Table C1. Gakkel Ridge

Depth (m)	Year	2011		2012		2015		2020		2021	
	Station	204		378		68		–		8	
	TTD parameter (years)	val	unc	val	unc	val	unc	val	unc	val	unc
300	Γ	27	4	28	2	23	2	NaN	NaN	31	2
	Δ	17	7	18	4	17	3	NaN	NaN	19	2
	t_{mode}	10	2	10	1	6	1	NaN	NaN	12	1
500	Γ	NaN	NaN	NaN	NaN	23	2	NaN	NaN	29	1
	D	NaN	NaN	NaN	NaN	16	3	NaN	NaN	17	2
	t_{mode}	NaN	NaN	NaN	NaN	7	1	NaN	NaN	12	1
1000	Γ	NaN	NaN	NaN	NaN	21	3	NaN	NaN	36	2
	D	NaN	NaN	NaN	NaN	21	5	NaN	NaN	28	4
	t_{mode}	NaN	NaN	NaN	NaN	3	1	NaN	NaN	9	1

Table C2. Amundsen Basin

Depth (m)	TTD parameter (years)	2011 / 218 val	unc	2012 / – val	unc	2015 / 81 val	unc	2020 / – val	unc	2021 / 16 val	unc	2021 / 20 val	unc
300	Γ	25	4	NaN	NaN	21	3	NaN	NaN	26	1	NaN	NaN
	Δ	22	8	NaN	NaN	21	6	NaN	NaN	15	2	NaN	NaN
	t_{mode}	5	1	NaN	NaN	3	1	NaN	NaN	11	1	NaN	NaN
500	Γ	NaN	NaN	NaN	NaN	23	3	NaN	NaN	27	2	26	2
	D	NaN	NaN	NaN	NaN	22	6	NaN	NaN	21	3	23	4
	t_{mode}	NaN	NaN	NaN	NaN	4	1	NaN	NaN	7	1	5	1
1000	Γ	NaN	NaN	NaN	NaN	11	3	NaN	NaN	32	2	30	2
	D	NaN	NaN	NaN	NaN	15	7	NaN	NaN	27	4	21	3
	t_{mode}	NaN	NaN	NaN	NaN	1	1	NaN	NaN	7	1	9	1

Table C3. Makarov Basin

Depth (m)	TTD parameter (years)	2011 / 226 val	unc	2012 / – val	unc	2015 / 101 val	unc	2020 / – val	unc	2021 / 28 val	unc
300	Γ	23	3	NaN	NaN	22	1	NaN	NaN	30	1
	Δ	9	4	NaN	NaN	11	3	NaN	NaN	16	2
	t_{mode}	15	2	NaN	NaN	11	2	NaN	NaN	14	1
500	Γ	NaN	NaN	NaN	NaN	26	2	NaN	NaN	31	1
	D	NaN	NaN	NaN	NaN	13	3	NaN	NaN	15	2
	t_{mode}	NaN	NaN	NaN	NaN	13	2	NaN	NaN	16	1
1000	Γ	NaN	NaN	NaN	NaN	47	2	NaN	NaN	42	1
	D	NaN	NaN	NaN	NaN	26	2	NaN	NaN	21	2
	t_{mode}	NaN	NaN	NaN	NaN	21	1	NaN	NaN	21	1

Table C4. Canada Basin

Depth (m)	TTD parameter (years)	2011 –		2012 –		2015 56		2020 CB5		2021 –	
		val	unc	val	unc	val	unc	val	unc	val	unc
	Γ	NaN	NaN	NaN	NaN	35	1	31	2	NaN	NaN
500	D	NaN	NaN	NaN	NaN	9	1	5	2	NaN	NaN
	t_{mode}	NaN	NaN	NaN	NaN	29	0	29	0	NaN	NaN

References

655   Alkire, M. B., Falkner, K. K., Rigor, I., Steele, M., and Morison, J.: The return of Pacific waters to the upper layers of the central Arctic Ocean, Deep Sea Research Part I: Oceanographic Research Papers, 54, 1509–1529, https://doi.org/10.1016/j.dsr.2007.06.004, 2007.

Alkire, M. B., Morison, J., and Andersen, R.: Variability in the meteoric water, sea-ice melt, and Pacific water contributions to the central Arctic Ocean, 2000-2014, Journal of Geophysical Research: Oceans, 120, 1573–1598, https://doi.org/10.1002/2014JC010023, 2015.

Alkire, M. B., Rember, R., and Polyakov, I.: Discrepancy in the Identification of the Atlantic/Pacific Front in the Central Arctic Ocean: NO
660   Versus Nutrient Relationships, Geophysical Research Letters, 46, 3843–3852, https://doi.org/10.1029/2018GL081837, 2019.

Anderson, L. G., Björk, G., Holby, O., Jutterström, S., Mörth, C. M., O'Regan, M., Pearce, C., Semiletov, I., Stranne, C., Stöven, T., Tanhua, T., Ulfsbo, A., and Jakobsson, M.: Shelf–Basin interaction along the East Siberian Sea, Ocean Science, 13, 349–363, https://doi.org/10.5194/os-13-349-2017, 2017.

Bauch, D., Van Der Loeff, M. R., Andersen, N., Torres-Valdes, S., Bakker, K., and Abrahamsen, E. P.: Origin of freshwater and polynya water
665   in the Arctic Ocean halocline in summer 2007, Progress in Oceanography, 91, 482–495, https://doi.org/10.1016/j.pocean.2011.07.017, 2011.

Broecker, W. S.: "NO", a conservative water-mass tracer, Earth and Planetary Science Letters, 23, 100–107, https://doi.org/10.1016/0012-821X(74)90036-3, 1974.

Casacuberta, N. and Smith, J. N.: Nuclear Reprocessing Tracers Illuminate Flow Features and Connectivity Between the Arctic and Subpolar
670   North Atlantic Oceans, Annual Review of Marine Science, 15, https://doi.org/10.1146/annurev-marine-032122-112413, 2022.

Casacuberta, N., Masqué, P., Henderson, G., Rutgers van-der Loeff, M., Bauch, D., Vockenhuber, C., Daraoui, A., Walther, C., Synal, H.-A., and Christl, M.: First ^{236}U data from the Arctic Ocean and use of ^{236}U/^{238}U and ^{129}I/^{236}U as a new dual tracer, Earth and Planetary Science Letters, 440, 127–134, https://doi.org/10.1016/j.epsl.2016.02.020, 2016.

Casacuberta, N., Christl, M., Vockenhuber, C., Wefing, A.-M., Wacker, L., Masqué, P., Synal, H.-A., and Rutgers van der Loeff, M.: Tracing
675   the Three Atlantic Branches Entering the Arctic Ocean With ^{129}I and ^{236}U, Journal of Geophysical Research: Oceans, 123, 6909–6921, https://doi.org/10.1029/2018JC014168, 2018.

Chamizo, E., Christl, M., López-Lora, M., Casacuberta, N., Wefing, A., and Kenna, T. C.: The Potential of 233U/236U as a Water Mass Tracer in the Arctic Ocean, Journal of Geophysical Research, 127, 12, https://doi.org/10.1029/2021JC017790, 2022.

Christl, M., Vockenhuber, C., Kubik, P., Wacker, L., Lachner, J., Alfimov, V., and Synal, H.-A.: The ETH Zurich AMS facilities: Performance
680   parameters and reference materials, Nuclear Instruments and Methods in Physics Research Section B: Beam Interactions with Materials and Atoms, 294, 29–38, https://doi.org/10.1016/j.nimb.2012.03.004, 2013.

Christl, M., Casacuberta, N., Lachner, J., Maxeiner, S., Vockenhuber, C., Synal, H.-A., Goroncy, I., Herrmann, J., Daraoui, A., Walther, C., and Michel, R.: Status of ^{236}U analyses at ETH Zurich and the distribution of ^{236}U and ^{129}I in the North Sea in 2009, Nuclear Instruments and Methods in Physics Research Section B: Beam Interactions with Materials and Atoms, 361, 510–516,
685   https://doi.org/10.1016/j.nimb.2015.01.005, 2015a.

Christl, M., Casacuberta, N., Vockenhuber, C., Elsässer, C., Bailly du Bois, P., Herrmann, J., and Synal, H.-A.: Reconstruction of the ^{236}U input function for the Northeast Atlantic Ocean: Implications for ^{129}I/^{236}U and ^{236}U/^{238}U-based tracer ages, Journal of Geophysical Research: Oceans, 120, 7282–7299, https://doi.org/10.1002/2015JC011116, 2015b.

Christl, M., Gautschi, P., Maxeiner, S., Müller, A. M., Vockenhuber, C., and Synal, H.-A.: 236U analyses with the ETH Zurich MILEA
690   prototype system, Nuclear Instruments and Methods in Physics Research Section B: Beam Interactions with Materials and Atoms, 534,
       61–71, https://doi.org/10.1016/j.nimb.2022.11.009, 2023.

Crameri, F.: Scientific colour maps, https://doi.org/10.5281/zenodo.8409685, 2023.

Dale, D., Christl, M., Vockenhuber, C., Macrander, A., Ólafsdóttir, S., Middag, R., and Casacuberta, N.: Tracing Ocean Circulation and
       Mixing From the Arctic to the Subpolar North Atlantic Using the^{129}I–^{236}U Dual Tracer, Journal of Geophysical Research: Oceans, 129,
695   e2024JC021 211, https://doi.org/10.1029/2024JC021211, 2024.

Edmonds, H.: Nuclear Fuel Reprocessing And Related Discharges, in: Encyclopedia of Ocean Sciences, pp. 1921–1928, Elsevier, ISBN
       978-0-12-227430-5, https://doi.org/10.1006/rwos.2001.0169, 2001.

Gascard, J.-C., Raisbeck, G., Sequeira, S., Yiou, F., and Mork, K. A.: The Norwegian Atlantic Current in the Lofoten basin inferred
       from hydrological and tracer data (^{129}I) and its interaction with the Norwegian Coastal Current, Geophysical Research Letters, 31,
700   https://doi.org/10.1029/2003GL018303, 2004.

GEBCO Compilation Group, .: GEBCO 2024 Grid, https://doi.org/10.5285/1c44ce99-0a0d-5f4f-e063-7086abc0ea0f, 2024.

Gerke, L., Arck, Y., and Tanhua, T.: Temporal Variability of Ventilation in the Eurasian Arctic Ocean, Journal of Geophysical Research:
       Oceans, 129, e2023JC020 608, https://doi.org/10.1029/2023JC020608, 2024.

Haine, T. W. N. and Hall, T. M.: A Generalized Transport Theory: Water-Mass Composition and Age, Journal of Physical Oceanography,
705   32, 1932–1946, https://doi.org/10.1175/1520-0485(2002)032<1932:AGTTWM>2.0.CO;2, 2002.

Heuzé, C., Karam, S., Muchowski, J., Padilla, A., Stranne, C., Gerke, L., Tanhua, T., Ulfsbo, A., Laber, C., and Stedmon, C. A.: Physical
       Oceanography during ODEN expedition SO21 for the Synoptic Arctic Survey, https://doi.org/10.1594/PANGAEA.951266, 2022a.

Heuzé, C., Karam, S., Muchowski, J., Padilla, A., Stranne, C., Gerke, L., Tanhua, T., Ulfsbo, A., Laber, C., and Stedmon,
       C. A.: Physical Oceanography measured on bottle water samples during ODEN expedition SO21 for the Synoptic Arctic Survey,
710   https://doi.org/10.1594/PANGAEA.951264, 2022b.

Karcher, M., Smith, J. N., Kauker, F., Gerdes, R., and Smethie, W. M.: Recent changes in Arctic Ocean circulation revealed by iodine-129
       observations and modeling, Journal of Geophysical Research: Oceans, 117, n/a–n/a, https://doi.org/10.1029/2011JC007513, 2012.

Khatiwala, S., Tanhua, T., Mikaloff Fletcher, S., Gerber, M., Doney, S., Graven, H. D., Gruber, N., McKinley, G., Murata, A., Rios, A., and
       Sabine, C. L.: Global ocean storage of anthropogenic carbon, Biogeosciences, 10, 2169–2191, https://doi.org/10.5194/bg-10-2169-2013,
715   2013.

Korhonen, M., Rudels, B., Marnela, M., Wisotzki, A., and Zhao, J.: Time and space variability of freshwater content, heat content and
       seasonal ice melt in the Arctic Ocean from 1991 to 2011, Ocean Science, 9, 1015–1055, https://doi.org/10.5194/os-9-1015-2013, 2013.

Kwok, R.: Arctic sea ice thickness, volume, and multiyear ice coverage: losses and coupled variability (1958–2018), Environmental Research
       Letters, 13, 105 005, iSBN: 1748-9326 Publisher: IOP Publishing, 2018.

720   Körtke, W., Walter, M., Huhn, O., Kanzow, T., and Rhein, M.: Decadal Changes in the Pathways of the Atlantic Water
       Core in the Arctic Ocean Inferred From Transient Tracers, Journal of Geophysical Research: Oceans, 129, e2024JC021 419,
       https://doi.org/10.1029/2024JC021419, 2024.

Lauvset, S. K., Lange, N., Tanhua, T., Bittig, H. C., Olsen, A., Kozyr, A., Álvarez, M., Azetsu-Scott, K., Brown, P. J., Carter, B. R., Cotrim
       Da Cunha, L., Hoppema, M., Humphreys, M. P., Ishii, M., Jeansson, E., Murata, A., Müller, J. D., Pérez, F. F., Schirnick, C., Steinfeldt,
725   R., Suzuki, T., Ulfsbo, A., Velo, A., Woosley, R. J., and Key, R. M.: The annual update GLODAPv2.2023: the global interior ocean
       biogeochemical data product, Earth System Science Data, 16, 2047–2072, https://doi.org/10.5194/essd-16-2047-2024, 2024.

Le Bras, I., Straneo, F., Muilwijk, M., Smedsrud, L. H., Li, F., Lozier, M. S., and Holliday, N. P.: How Much Arctic Fresh Water Participates in the Subpolar Overturning Circulation?, Journal of Physical Oceanography, 51, 955–973, https://doi.org/10.1175/JPO-D-20-0240.1, 2021.

Marnela, M., Rudels, B., Olsson, K. A., Anderson, L. G., Jeansson, E., Torres, D. J., Messias, M.-J., Swift, J. H., and Watson, A. J.: Transports of Nordic Seas water masses and excess SF6 through Fram Strait to the Arctic Ocean, Progress in Oceanography, 78, 1–11, https://doi.org/10.1016/j.pocean.2007.06.004, 2008.

Morison, J., Kwok, R., Peralta-Ferriz, C., Alkire, M., Rigor, I., Andersen, R., and Steele, M.: Changing Arctic Ocean freshwater pathways, Nature, 481, 66–70, https://doi.org/10.1038/nature10705, 2012.

Newton, R., Schlosser, P., Mortlock, R., Swift, J., and MacDonald, R.: Canadian Basin freshwater sources and changes: Results from the 2005 Arctic Ocean Section, Journal of Geophysical Research: Oceans, 118, 2133–2154, https://doi.org/10.1002/jgrc.20101, 2013.

Paffrath, R., Laukert, G., Bauch, D., Rutgers van der Loeff, M., and Pahnke, K.: Separating individual contributions of major Siberian rivers in the Transpolar Drift of the Arctic Ocean, Scientific Reports, 11, 8216, https://doi.org/10.1038/s41598-021-86948-y, tex.ids= paffrathSeparatingIndividualContributions2021a, 2021.

Pasqualini, A., Schlosser, P., Newton, R., Smethie Jr, W. M., and Friedrich, R.: A Multi-Decade Tracer Study of the Circulation and Spreading Rates of Atlantic Water in the Arctic Ocean, Journal of Geophysical Research: Oceans, 129, https://doi.org/10.1029/2023JC020738, 2024.

Payne, A., Wefing, M., Christl, M., Vockenhuber, C., Williams, W., Smith, J. N., and Casacuberta, N.: Circulation Timescales and Pathways of Atlantic Water in the Canada Basin: Insights From Transient Tracers 129I and 236U, Journal of Geophysical Research, 2024.

Polyakov, I. V., Beszczynska, A., Carmack, E. C., Dmitrenko, I. A., Fahrbach, E., Frolov, I. E., Gerdes, R., Hansen, E., Holfort, J., Ivanov, V. V., Johnson, M. A., Karcher, M., Kauker, F., Morison, J., Orvik, K. A., Schauer, U., Simmons, H. L., Skagseth, Ø., Sokolov, V. T., Steele, M., Timokhov, L. A., Walsh, D., and Walsh, J. E.: One more step toward a warmer Arctic, Geophysical Research Letters, 32, https://doi.org/10.1029/2005GL023740, 2005.

Polyakov, I. V., Pnyushkov, A. V., Alkire, M. B., Ashik, I. M., Baumann, T. M., Carmack, E. C., Goszczko, I., Guthrie, J., Ivanov, V. V., Kanzow, T., Krishfield, R., Kwok, R., Sundfjord, A., Morison, J., Rember, R., and Yulin, A.: Greater role for Atlantic inflows on sea-ice loss in the Eurasian Basin of the Arctic Ocean, Science, 356, 285–291, https://doi.org/10.1126/science.aai8204, 2017.

Polyakov, I. V., Rippeth, T. P., Fer, I., Alkire, M. B., Baumann, T. M., Carmack, E. C., Ingvaldsen, R., Ivanov, V. V., Janout, M., Lind, S., Padman, L., Pnyushkov, A. V., and Rember, R.: Weakening of Cold Halocline Layer Exposes Sea Ice to Oceanic Heat in the Eastern Arctic Ocean, Journal of Climate, 33, 8107–8123, https://doi.org/10.1175/JCLI-D-19-0976.1, 2020.

Polyakov, I. V., Ingvaldsen, R. B., Pnyushkov, A. V., Bhatt, U. S., Francis, J. A., Janout, M., Kwok, R., and Skagseth, Ø.: Fluctuating Atlantic inflows modulate Arctic atlantification, Science, 381, 972–979, https://doi.org/10.1126/science.adh5158, 2023.

Polyakov, I. V., Pnyushkov, A. V., Charette, M., Cho, K.-H., Jung, J., Kipp, L., Muilwijk, M., Whitmore, L., Yang, E. J., and Yoo, J.: Atlantification advances into the Amerasian Basin of the Arctic Ocean, Science Advances, 11, eadq7580, https://doi.org/10.1126/sciadv.adq7580, 2025.

Proshutinsky, A., Dukhovskoy, D., Timmermans, M.-L., Krishfield, R., and Bamber, J. L.: Arctic circulation regimes, Philosophical Transactions of the Royal Society A: Mathematical, Physical and Engineering Sciences, 373, 20140 160, https://doi.org/10.1098/rsta.2014.0160, 2015.

Pérez-Tribouillier, H., Jaccard, S. L., Blaser, P., Christl, M., Creac'h, L., Hölemann, J., Scheiwiller, M., Vockenhuber, C., Wefing, A., and Casacuberta, N.: The Role of the St. Anna Trough in Atlantic Water Transport into the Arctic Ocean: A Novel Radiogenic Isotope Assessment Using Iodine, Uranium, and Neodymium. Under review in Journal of Geophysical Research: Oceans.

Raimondi, L., Tanhua, T., Azetsu-Scott, K., Yashayaev, I., and Wallace, D.: A 30 -Year Time Series of Transient Tracer-Based Estimates of Anthropogenic Carbon in the Central Labrador Sea, Journal of Geophysical Research: Oceans, 126, https://doi.org/10.1029/2020JC017092, 2021.

Raimondi, L., Wefing, A., and Casacuberta, N.: Anthropogenic Carbon in the Arctic Ocean: Perspectives From Different Transient Tracers, Journal of Geophysical Research: Oceans, 129, e2023JC019 999, https://doi.org/10.1029/2023JC019999, 2024.

Rantanen, M., Karpechko, A. Y., Lipponen, A., Nordling, K., Hyvärinen, O., Ruosteenoja, K., Vihma, T., and Laaksonen, A.: The Arctic has warmed nearly four times faster than the globe since 1979, Communications Earth & Environment, 3, 168, https://doi.org/10.1038/s43247-022-00498-3, 2022.

Rudels, B.: Arctic Ocean circulation, processes and water masses: A description of observations and ideas with focus on the period prior to the International Polar Year 2007–2009, Progress in Oceanography, 132, 22–67, https://doi.org/10.1016/j.pocean.2013.11.006, 2015.

Rudels, B., Anderson, L. G., and Jones, E. P.: Formation and evolution of the surface mixed layer and halocline of the Arctic Ocean, Journal of Geophysical Research: Oceans, 101, 8807–8821, https://doi.org/10.1029/96JC00143, 1996.

Schulz, K., Koenig, Z., Muilwijk, M., Bauch, D., Hoppe, C. J. M., Droste, E. S., Hoppmann, M., Chamberlain, E. J., Laukert, G., Stanton, T., Quintanilla-Zurita, A., Fer, I., Heuzé, C., Karam, S., Mieruch-Schnülle, S., Baumann, T. M., Vredenborg, M., Tippenhauer, S., and Granskog, M. A.: The Eurasian Arctic Ocean along the MOSAiC drift in 2019–2020: An interdisciplinary perspective on physical properties and processes, Elem Sci Anth, 12, 00 114, https://doi.org/10.1525/elementa.2023.00114, 2024.

Smith, J. N., McLaughlin, F. A., Smethie, W. M., Moran, S. B., and Lepore, K.: Iodine-129, ^{137}Cs, and CFC-11 tracer transit time distributions in the Arctic Ocean, Journal of Geophysical Research, 116, https://doi.org/10.1029/2010JC006471, 2011.

Smith, J. N., Karcher, M., Casacuberta, N., Williams, W. J., Kenna, T., and Smethie, W. M.: A Changing Arctic Ocean: How Measured and Modeled [129]I Distributions Indicate Fundamental Shifts in Circulation Between 1994 and 2015, Journal of Geophysical Research: Oceans, 126, https://doi.org/10.1029/2020JC016740, 2021.

Smith, J. N., Smethie, W. M., and Casacuberta, N.: Synoptic [129]I and CFC–SF_6 Transit Time Distribution (TTD) Sections Across the Central Arctic Ocean From the 2015 GEOTRACES Cruises, Journal of Geophysical Research: Oceans, 127, https://doi.org/10.1029/2021JC018120, 2022.

Snoeijs-Leijonmalm, P., , and the SAS-Oden 2021 Scientific Party: Expedition Report SWEDARCTIC Synoptic Arctic Survey 2021 with icebreaker Oden, Tech. rep., Swedish Polar Research Secretariat, 2022.

Stöven, T. and Tanhua, T.: Ventilation of the Mediterranean Sea constrained by multiple transient tracer measurements, Ocean Science, 10, 439–457, https://doi.org/10.5194/os-10-439-2014, 2014.

Stöven, T., Tanhua, T., Hoppema, M., and Bullister, J. L.: Perspectives of transient tracer applications and limiting cases, Ocean Science, 11, 699–718, https://doi.org/10.5194/os-11-699-2015, 2015.

Stöven, T., Tanhua, T., Hoppema, M., and von Appen, W.-J.: Transient tracer distributions in the Fram Strait in 2012 and inferred anthropogenic carbon content and transport, Ocean Science, 12, 319–333, https://doi.org/10.5194/os-12-319-2016, 2016.

Tanhua, T., Jones, E. P., Jeansson, E., Jutterström, S., Smethie, W. M., Wallace, D. W. R., and Anderson, L. G.: Ventilation of the Arctic Ocean: Mean ages and inventories of anthropogenic CO_2 and CFC-11, Journal of Geophysical Research, 114, https://doi.org/10.1029/2008JC004868, 2009.

Thyng, K., Greene, C., Hetland, R., Zimmerle, H., and DiMarco, S.: True Colors of Oceanography: Guidelines for Effective and Accurate Colormap Selection, Oceanography, 29, 9–13, https://doi.org/10.5670/oceanog.2016.66, 2016.

Vockenhuber, C., Casacuberta, N., Christl, M., and Synal, H.-A.: Accelerator Mass Spectrometry of ^{129}I towards its lower limits, Nuclear Instruments and Methods in Physics Research Section B: Beam Interactions with Materials and Atoms, 361, 445–449, https://doi.org/10.1016/j.nimb.2015.01.061, 2015.

Wang, Q., Shu, Q., and Wang, F.: Recent emergence of Arctic atlantification dominated by climate warming, Science Advances, 10, eadq5235, https://doi.org/10.1126/sciadv.adq5235, 2024.

Waugh, D. W., Hall, T. M., and Haine, T. W. N.: Relationships among tracer ages, Journal of Geophysical Research, 108, https://doi.org/10.1029/2002JC001325, 2003.

Waugh, D. W., Hall, T. M., Mcneil, B. I., Key, R., and Matear, R. J.: Anthropogenic CO_2 in the oceans estimated using transit time distributions, Tellus B: Chemical and Physical Meteorology, 58, 376–389, https://doi.org/10.1111/j.1600-0889.2006.00222.x, 2006.

Wefing, A.-M.: I-129 and U-236 data from the ODEN expedition SO21 for the Synoptic Arctic Survey, https://doi.org/10.5281/zenodo.15056897, 2025.

Wefing, A.-M., Casacuberta, N., Christl, M., Gruber, N., and Smith, J. N.: Circulation timescales of Atlantic Water in the Arctic Ocean determined from anthropogenic radionuclides, Ocean Science, 17, 111–129, https://doi.org/10.5194/os-17-111-2021, 2021.

Wefing, A.-M., Casacuberta, N., Christl, M., and Dodd, P. A.: Water mass composition in Fram Strait determined from the combination of 129I and 236U: Changes between 2016, 2018, and 2019, Frontiers in Marine Science, p. 16, https://doi.org/10.3389/fmars.2022.973507, 2022.

Whitmore, L. M., Pasqualini, A., Newton, R., and Shiller, A. M.: Gallium: A New Tracer of Pacific Water in the Arctic Ocean, Journal of Geophysical Research: Oceans, 125, https://doi.org/10.1029/2019JC015842, 2020.

Östlund, H. G. and Hut, G.: Arctic Ocean water mass balance from isotope data, Journal of Geophysical Research, 89, 6373, https://doi.org/10.1029/JC089iC04p06373, rEAD, 1984.